Sister chromatid cohesion is mediated by individual cohesin complexes

Fena Ochs[1,2,*], Charlotte Green[1], Aleksander Tomasz Szczurek[1], Lior Pytowski[3], Sofia Kolesnikova[4,5], Jill Brown[6], Daniel Wolfram Gerlich[4], Veronica Buckle[6], Lothar Schermelleh[1] and Kim Ashley Nasmyth[1,*]

[1]Department of Biochemistry, University of Oxford, South Parks Road, Oxford, OX1 3QU, United Kingdom

[2]Present address: Biotech Research and Innovation Centre, Faculty of Health and Medical Sciences, University of Copenhagen, 2200 Copenhagen, Denmark

[3]Sir William Dunn School of Pathology, University of Oxford, Oxford, OX1 3RE, United Kingdom

[4]Institute of Molecular Biotechnology of the Austrian Academy of Sciences (IMBA), Vienna BioCenter (VBC), Vienna, Austria

[5]Vienna BioCenter PhD Program, Doctoral School of the University of Vienna and Medical University of Vienna, Vienna, Austria

[5]MRC Weatherall Institute of Molecular Medicine, University of Oxford, Oxford, OX3 9DS, United Kingdom

*Corresponding author: fena.ochs@bric.ku.dk and ashley.nasmyth@bioch.ox.ac.uk

ABSTRACT

Eukaryotic genomes are organized by loop extrusion and sister chromatid cohesion, both mediated by the multimeric cohesin protein complex. Understanding how cohesin holds sister DNAs together, and how loss of cohesion causes age-related infertility in females, requires knowledge as to cohesin's stoichiometry *in vivo*. Using quantitative super-resolution imaging, we identify two discrete populations of chromatin bound cohesin in post-replicative human cells. While most complexes appear dimeric, cohesin localized to sites of sister chromatid cohesion and associated with sororin is exclusively monomeric. The monomeric stoichiometry of sororin:cohesin complexes demonstrates that sister chromatid cohesion is conferred by individual cohesin rings, a key prediction of the proposal that cohesion arises from their co-entrapment of sister DNAs.

ONE-SENTENCE SUMMARY

The sister chromatid cohesion necessary for faithful cell division is mediated by individual cohesin rings.

Cohesin holds sister DNAs together from S phase until anaphase, which is known as sister chromatid cohesion (SCC) (*1*). Besides facilitating double strand break repair during G2 (*2*, *3*), SCC is necessary for the traction by microtubules of kinetochore pairs in opposite directions, a process essential for chromosome segregation during both meiosis and mitosis (*4*). In addition to SCC, cohesin mediates loop extrusion (LE) (*4*, *5*), important for bringing together certain enhancers and their cognate promoters (*6*)

The core of cohesin is a tripartite ring formed by a kleisin subunit called RAD21$^{Scc1/Mcd1}$ and a pair of rod-shaped SMC proteins, SMC1 and SMC3 (*7*, *8*). The discovery that apo-cohesin forms a tripartite ring whose integrity is destroyed at the onset of anaphase through RAD21's cleavage by Separase (*9*) led to the suggestion that cohesion is mediated through the entrapment of sister DNAs within individual cohesin rings, known as the ring model (*4*, *10*).

Though the sister minichromosome DNA co-entrapment measured by cross-linking is a feature of individual cohesin rings (*11–13*), three different types of observation have led to suggestions that chromosomal cohesion is in fact conferred by the pair-wise interaction of cohesin rings associated with individual sister chromatids, known as the handcuff model (*14*, *15*). The first involves mammalian cell lines expressing differently tagged versions of cohesin's RAD21 subunit and the demonstration that immuno-precipitation of one type is accompanied by co-purification of the other (*16*). Interaction between cohesin rings has likewise been detected in yeast using a proximity-dependent modification assay (*17*). The second is the finding that loss of cohesion upon inactivation of its PDS5 subunit is not accompanied by any reduction in the amount of cohesin associated with chromosomes, which has led to the suggestion that, though not required for cohesin's association with or indeed entrapment of individual chromatids, PDS5 is nevertheless necessary for linking rings associated with each sister (*18*). The last is the finding that otherwise lethal mutations in one allele of RAD21's yeast homologue Scc1 complement the lethality caused by a different allele associated with its homologue. To explain this "inter-allelic" complementation, it has been suggested that the two different alleles affect different aspects of Scc1 function and that dimeric cohesin complexes composed of different alleles possess both functions, albeit provided by different Scc1 molecules (*19*). Though all three sets of observations are consistent with the handcuff model, none of them directly addresses whether sister chromatid cohesion *per se* requires interaction between cohesin rings. Even if it does indeed exist, ring dimerization could be a feature of cohesin complexes engaged in activities other than cohesion, such as loop extrusion.

The notion that multimerization may have little or nothing to do with cohesion *per se* is supported by super-resolution imaging of Rec8 in spreads from meiotic prophase in *C. elegans* (*20*). Rec8 is a meiotic kleisin that is essential for cohesion but not for meiotic axis formation. In animals expressing both GFP- or Flag-tagged versions as the sole form of Rec8, few if any foci of fluorescence co-localize. Moreover, the intensity of most Rec8-GFP foci corresponds to that of individual GFP molecules. That said, these observations do not exclude the possibility that cohesive complexes are only a minority of those detected, which may include loop extruding Rec8 complexes. In other words,

these observations did not observe directly a cohesin population associated with demonstrable cohesion sites.

Given that only a fraction of chromosomal cohesin is involved in sister chromatid cohesion (*21*), the challenge in determining cohesive cohesin's stoichiometry is how to image this subpopulation. The dependence of cohesion in animal cells on a protein called sororin (*22*) offers a potentially unique opportunity. Sororin is a short, largely unstructured protein that, though present in many eukaryotic lineages, including some fungi, most higher plants, and most but not all animals (*22*, *23*), is poorly conserved except for a C-terminal "sororin" motif (*22*). In mammalian cells and plants, sororin associates with chromosomal cohesin during S phase and is essential for maintaining cohesion thereafter (*22*, *23*). It has been suggested that the sororin motif forms a short alpha helix that binds the RAD21:SMC3 neck interface, an interaction that might hinder the dissociation of RAD21 from SMC3 necessary for release (*24*). Though sororin's properties (*25–27*) raise the possibility that it might bind only to cohesive cohesin, and if so, could act as a marker for this population, it is also possible that sororin binds non-cohesive as well as cohesive cohesin, despite being dispensable for loop extrusion *in vitro* (*5*, *28*).

We sought to investigate whether sororin is a specific marker for cohesive cohesin and if so, employ super-resolution imaging of cultured human cells to assess the stoichiometry of chromatin bound cohesin at sites of sister chromatid cohesion.

RESULTS

Chromatin-bound cohesin exists in both monomeric and dimeric states

To determine the stoichiometry of chromatin bound cohesin complexes in intact cells, we developed a quantitative super-resolution imaging approach based on 3D-structured illumination microscopy (3D-SIM) (*29*, *30*), which allows visualization of cohesin on chromatin and inside structurally preserved human cells. We confined our analysis to chromatin bound cohesin using a mild pre-extraction protocol to remove soluble proteins and focused on G2 cells, where loop extrusion and sister chromatid cohesion co-exist. To image cohesin, we used human osteosarcoma U2OS cells in which a HaloTag had been inserted into all alleles of RAD21 (*31*) (**Fig. 1A**). In contrast to conventional microscopy, 3D-SIM reveals small and well-separated cohesin spot signals, due to its greater volumetric resolution and enhanced contrast (**Fig. 1B, Fig. 1SA**) (*32*).

Quantitation of fluorescent RAD21 spots produced with the JFX554 dye revealed three discrete populations (**Fig. 1B, C**). To determine their precise stoichiometry, we reduced the dye concentration during labeling to 0.05% of saturating conditions, thereby creating a population of spots that should correspond to individual RAD21 molecules (**Fig. 1D**). Using highly inclined and laminated optical sheet microscopy (HILO), these sparse spots were bleached in a single step, confirming their monomeric nature (**Fig. 1E, Fig. S1B-D**). The volumes of this "monomeric" RAD21 matched the first population of total chromatin bound RAD21 (**Fig. 1F**). Using this calibration, we estimate that 22% of G2 chromosomal

cohesin is monomeric, 61% appeared dimeric, and the remaining 17% was initially classified as multimeric.

To confirm that the RAD21 spots correspond to cohesin, we homozygously inserted a Spot-tag in SMC3's hinge domain, to omit inserting a second tag close to cohesin's ATP heads, where all N- and C-termini of cohesin come together. The doubly tagged cell line (**Fig. S2A-D)** had normal cell cycle progression, sister chromatid cohesion and loop extrusion (**Fig. S2E-J**). We tested whether chromatin bound RAD21 corresponds to actual cohesin complexes, by measuring colocalization between RAD21 and SMC3. To this end, we developed SIMinspector, an open-access image analysis tool for colocalization analysis in 3D- super-resolution images (**Fig. S3A-F**; see Methods). Using SIMinspector, we measured the association of chromatin bound RAD21 with SMC3, which yielded 89.1 ± 1.5% colocalization (**Fig. S4A-C**), implying that most if not all RAD21 foci correspond to actual cohesin complexes.

Sororin occupies sites of *trans* chromatid contacts

One way of addressing whether either monomeric or dimeric populations correspond to cohesive cohesin would be to determine whether they are associated with sororin. However, this would only be a valid approach if one were certain that sororin is present at cohesion sites and not merely a factor associated with numerous types of cohesin including one that happens to be necessary for cohesion. We therefore compared the genomic distribution of cohesin and sororin measured by chromatin immunoprecipitation sequencing (ChIP-Seq) with the frequency of sister chromatid contacts mapped by sister chromatid-sensitive (scs)-HiC (*33*) (**Fig.2A**). First, we detected all cohesin accumulation sites genome-wide by calling peaks in published SMC3 ChIP-Seq data from G2-synchronized cells (*27*) . We then used sororin ChiP-Seq data from the same study to classify SMC3 peaks according to the presence or absence of sororin (**Fig. 2B, C**). We then calculated average contact probability maps around both types of regions, separately for *cis*-sister-contacts representing DNA loops and for *trans*-sister contacts. *Cis*-contact maps showed abundant interactions extending away from SMC3 sites containing sororin as well as those lacking sororin, indicating the loop-forming cohesin is present at both types of loci (**Fig. 2D, E**). *Trans*-contact maps, in contrast, were associated with increased contacts around SMC3 sites containing sororin, but not around those lacking it (**Fig. 2D, E**). Profiling trans contact densities at individual genomic regions confirmed that the concentration of *trans*-contacts around SMC3 sites containing sororin occurred throughout the genome (**Fig. 2F, G**). In other words, trans contacts were found in the vicinity of cohesin associated with sororin but not with cohesin lacking it.

Cohesin complexes associated with sororin specifically mark sites of sister chromatid cohesion

Though consistent with the notion that sororin is exclusively present at cohesion sites, data from populations of cells cannot *per se* demonstrate that sororin is actually present at sites where sisters are held together by cohesin. To do this, it would be necessary to measure sister cohesion of particular genomic sequences as well as their association with sororin within individual cells (**Fig. 3A**). To identify a site of cohesion using

fluorescence in situ hybridization (FISH) we employed a cosmid DNA probe library covering 2 Mb of telomeric chromosome band 16p13.3 (*34*). 30 cosmid probes were labelled spaced on average every 75 kb midpoint to midpoint to cover coordinates 266 kb to 1922 kb from the telomere and four more cosmids were labelled to extend the analysis by a further 1.5 Mb, to approximately 3.5 Mb from the telomere. FISH was carried out in a human lymphoblastoid cell line established from a normal individual (TA) and a mouse erythroleukemia hybrid cell line containing a normal human chromosome 16 (MEL JY5.4).

Initially, using conventional microscopy, we analyzed whether sister DNAs appeared as "split dots", namely distinct fluorescent signals for each sister, or as single signals, indicating spatial proximity of sisters. This revealed, in both cell lines, a 320 kb interval within which greater than 60% of sister DNAs were closely juxtaposed (**Fig. 3B**). To address whether juxtaposition was cohesin dependent and associated with sororin, we combined super-resolution imaging of sororin in U2OS G2 cells with resolution after single-strand exonuclease resection (RASER)-FISH, which allows visualization of DNA sequences in structurally preserved cells by a method that avoids heat denaturation or acid treatment (**Fig. 3A**) (*35*). Analysis of two probes HS306A4 (probe midpoint 898 kb) and HS443D9 (probe midpoint 955 kb) within the interval using 3D-SIM showed that sister DNAs were present either as "sausage" or "dumbbell" shaped single territories in approximately 70% of analyzed alleles (HS443D9 69.13 ± 9.38%; HS306A4 71.28 ± 2.9%), but segregated into distinct territories in the remainder (**Fig. 3C; Fig. S5a**). The presence of both sisters within a single territory in most cases was consistent with the data using conventional FISH from TA and MELY J5.4 cells (**Fig. 3B)**. The greater resolution achieved using RASER-FISH combined with 3D-SIM revealed that even when sister DNAs are closely juxtaposed, the signals were not uniform within each territory but instead concentrated at opposite poles of elongated territories, suggesting that sister sequences occupy distinct positions even in those cells where they are closely juxtaposed. Sister DNA juxtaposition was greatly reduced by degradation of the Halo-tagged RAD21 following an 8-hour PROTAC (proteolysis targeting chimera) 3 treatment (**Fig. S5B**), which caused the appearance of "split dots" in >90% of cases (HS443D9 97.68 ± 3.29%; HS306A4 87.61 ± 7.43%) (**Fig. 3C**). It also resulted in a spatial separation of sister DNAs from <500 nm to up to 1.5 μm (**Fig. S5C**). When analyzing sororin, we observed colocalization with closely juxtaposed sisters in >95% of cases but rarely with either sister when (in different G2 cells) they were clearly separate (**Fig. 3D**). Likewise, distance measurements of sister signals revealed a strong correlation between sororin presence and the spatial coupling of sister DNAs. Thus, DNA loci with and without sororin have average distances of 116 ± 68 nm and 233 ± 103 nm respectively (**Fig. 3E**). The colocalization of sororin with this genomic site was also detected in ChIP-Seq analysis, which showed discrete accumulation of both cohesin, marked by SMC3, and sororin at this locus (**Fig. S5D**).

These findings suggest that sororin is not merely required for holding sisters together but is exclusively associated with cohesive cohesin and therefore a suitable marker to study this subpopulation.

Sororin is a monomer and associated with <1/3 of chromatin bound cohesin

To assess the oligomerization state of cohesive cohesin, we used 3D-SIM to image chromatin bound cohesin (RAD21-Halo) and sororin (antibody) in G2 U2OS cells (**Fig. 4A**). We first analyzed the status of sororin, whose foci were sparse and had a uniform Gaussian intensity distribution (**Fig. 4B, C**). To measure their stoichiometry, we used fluorescent signals from primary-secondary antibody conjugates binding non-specifically to the glass surface outside cells to calibrate those associated with chromatin within cells. The distribution of single primary-secondary antibody conjugates fell exactly into the chromatin bound sororin distribution (**Fig. 4D, E**), implying that the majority of chromatin bound sororin is monomeric (74.4%). The remaining 25.6% were initially classified as multimeric. To confirm the specificity of our antibody, we analyzed the cell cycle distribution of chromatin bound sororin using high-content widefield microscopy (quantitative image-based cytometry, QIBC) (*36*, *37*). Specifically, we classified cell cycle stages based on EdU pulse-labeling, DNA content and MCM2 immunofluorescence, and co-staining of chromatin bound sororin showed its absence on G1 chromatin and accumulation from early S phase onwards, increasing to G2, consistent with previous reports (**Fig. S6A, B**) (*25*). We also confirmed that RNAi-mediated depletion of sororin abrogated the western blot signal (**Fig. S6C**). To determine the stoichiometry of chromatin bound sororin using an independent method, we added a C-terminal SNAP tag homozygously to the endogenous locus in the previously established RAD21-Halo, SMC3-E602-Spot U2OS cell line (**Fig. S6E, F**). The distribution of the dye-labelled sororin-SNAP resembled antibody-detected sororin regarding chromatin recruitment during cell cycle (**Fig. S6F**). Step-wise photobleaching of SNAP-tagged sororin revealed 1-step bleaching in 92.5 ± 4.7% of cases (**Fig. S6H**), confirming that the majority of chromatin bound sororin is present as a monomer.

Having demonstrated that chromosomal sororin is localized exclusively at cohesion sites and that it exists predominantly as individual molecules, we addressed its association with cohesin. We used SIMinspector to analyze the association in G2 cells of sororin with chromatin bound cohesin marked by RAD21-Halo. This showed that 28.5 ± 0.064% of chromatin bound cohesin co-localizes with sororin (**Fig. 4F, G**), a proportion that matches the fraction of cohesin stably associated with chromatin in G2 phase HeLa cells, estimated using fluorescence recovery after photobleaching (FRAP) (*21*, *27*).

Sister chromatid cohesion is maintained by individual cohesin rings

To ascertain whether the cohesin complexes associated with sororin correspond to monomers, dimers, or multimers, we developed a labeling strategy to differentiate monomeric and multimeric proteins by 3D-SIM, utilizing the fact that each HaloTag can only bind a single dye ligand. Using our RAD21-Halo cell line, we determined conditions in which about half the RAD21-Halo molecules were labelled with one and the other half with a second dye and only very few were unlabeled. If under these conditions, sororin were associated with cohesin monomers then we should never observe co-localization of the two dyes, whereas if it were associated with dimers, then we should observe colocalization in 50% of cases (**Fig. 5A**). To implement this, we determined the concentrations of the HaloTag dyes JFX554 and JFX650 necessary to saturate labeling when on their own and subsequently the concentrations necessary to obtain equal labeling when combined (**Fig. S7A**). The extent of RAD21-Halo molecules that were

unlabeled was then measured by a chase with a third dye. Using these conditions (**Fig. S7B, C**), we co-stained for sororin and measured the frequency of co-localization with neither, one or the other, or both Halo dyes. Given that we had previously identified monomeric, dimeric, and multimeric fractions of chromatin bound cohesin (**Fig. 1C**), there were four potential outcomes of this experiment, with either monomers, dimers, multimers or a mix of fractions enriched at cohesion sites labelled by sororin (**Fig. 5A**) and an equivalent set at sites lacking it. Sororin signals were detected with neither dye (8.21%), with dye 1 alone (JFX554, 45.00%), or with dye 2 alone (JFX650, 44.46%) (**Fig. 5B-F**). They were observed to colocalize with both Halo dyes in only 2.33% of cases (**Fig. 5C, D**) and inspection revealed these instances consisted of a pair of close but clearly separate sororin molecules, each associated with a RAD21-Halo molecule labeled with only a single dye (**Fig. S7D**). The observed distribution implies that sites of chromatid cohesion marked by single molecules of sororin are associated with a monomeric form of cohesin. It also shows that most if not all chromatin bound sororin co-localizes with cohesin in G2, as less than 10% of sororin were detected without a cohesin partner.

In the case of sororin-free cohesin signals, 26.67% were labelled with dye #1 (JFX554), 24.79% with dye #2 (JFX650) and 48.54% with both dyes (JFX554 and JFX650) (**Fig.5E, F**), a distribution expected for dimeric complexes (**Fig. 5A**) and ruling out an appreciable fraction of multimeric (>2) complexes. To explain this, we suggest that the multimeric complexes revealed in **Figure 1** may have arisen due to the limited resolution intrinsic in single dye labeling. With the dual dye labeling shown in **Figure 5**, many of the complexes classified as multimeric in **Figure 1** are resolved into a mixture of monomers and dimers.

These observations suggest that chromatin bound cohesin exists in two discrete populations; cohesive cohesin which is monomeric and non-cohesive cohesin, which appears dimeric, at least at the resolution of our imaging. To check by independent means whether cohesive cohesin is indeed monomeric, we used two additional approaches. First, we segmented the volumes of sororin-associated cohesin and overlaid it with the fluorescence volume distributions for all chromatin bound cohesin shown before (**Fig. S7E**). This revealed that sororin-associated cohesin has a volume of a cohesin monomer. Secondly, we combined our dye mixing experiment with RASER-FISH visualization of sister DNAs, thereby permitting us to determine the stoichiometry of cohesin at sites marked by close spatial proximity between sister chromatids and sororin presence. This revealed that sites of cohesion, defined by their association with sororin and sister DNA proximity, were invariably labelled with either one or the other dye but never with both (**Fig. 5G**).

We conclude that sister chromatid cohesion in post-replicative cells is maintained by individual cohesin rings. Of note, the observed lack of dimers at cohesion sites is not due either to the absence of such complexes within cells or our inability to detect them, because the majority of G2 cohesin not engaged in cohesion is observably dimeric. Future studies will be required to address whether this non-cohesive dimeric fraction corresponds to cohesin actively engaged in loop extrusion, in which case it should contain NIPBL, or to cohesin that has already translocated and halted at CTCF sites where it presumably contains PDS5 (**Fig. S8**).

DISCUSSION

Our finding that cohesion is mediated by monomeric cohesin is in line with findings in *C.elegans* chromosomes during meiosis I (*20*), raising the possibility that cohesion mediated by monomeric cohesin is a universal principle.

While our data excludes models where cohesin mutlimers mediate cohesion, we nevertheless found a large fraction of non-cohesive complexes that are closely juxtaposed with a neighboring complex. Whether these complexes correspond to true dimers or spatially close complexes will require imaging at even higher resolution as well as elucidation of the mechanism of dimerization. We note that Alphafold multimer predicts that cohesin's accessory components NIPBL and SA bind each other via two independent interfaces (*24*). If such interactions were to occur between proteins bound to different SMC-kleisin rings, then they would create cohesin dimers held together in a tetravalent, and hence robust, manner. A key question is therefore whether dimeric complexes correspond to cohesin occupied by NIPBL and whether they might therefore be engaged in loop extrusion.

Our conclusion that sororin is not only required for cohesion but actually marks cohesin as cohesive has an important corollary. We estimate that somewhere between a quarter and a third of chromosomal cohesin complexes are associated with sororin during G2, which agrees with the finding that a similar fraction is very stably bound to chromosomes in G2 in a manner dependent on sororin (*21*, *27*, *38*). It has been estimated that around 100,000 cohesin complexes are bound to the chromosomes of a diploid cell (*21*). If of these at least 25,000 are cohesive, this equates to one cohesive cohesin complex on average every 240 kbp. Thus, up to four cohesive complexes would be found within the average TAD, which contains 1.15 Mbp.

There is now extensive information about the structure of cohesin rings (*24*). In addition, there is clear evidence that neither NIPBL (*39*) nor PDS5 (*40*) are strictly necessary for holding sisters together. This along with our finding that cohesive cohesin is monomeric greatly reduced the possible mechanisms of how sister chromatid cohesion can be established during DNA replication.

REFERENCES

1. S. Yatskevich, J. Rhodes, K. Nasmyth, Organization of Chromosomal DNA by SMC Complexes. *Annu. Rev. Genet.* **53**, 1–38 (2019).

2. C. Sjögren, K. Nasmyth, Sister chromatid cohesion is required for postreplicative double-strand break repair in Saccharomyces cerevisiae. *Curr. Biol.* **11**, 991–995 (2001).

3. L. Ström, H. B. Lindroos, K. Shirahige, C. Sjögren, Postreplicative Recruitment of Cohesin to Double-Strand Breaks Is Required for DNA Repair. *Mol. Cell* **16**, 1003–1015 (2004).

4. K. Nasmyth, DISSEMINATING THE GENOME: Joining, Resolving, and Separating Sister Chromatids During Mitosis and Meiosis. *Annu. Rev. Genet.* **35**, 673–745 (2001).

5. I. F. Davidson, B. Bauer, D. Goetz, W. Tang, G. Wutz, J.-M. Peters, DNA loop extrusion by human cohesin. *Science* **366**, 1338–1345 (2019).

6. M. A. Karpinska, A. M. Oudelaar, The role of loop extrusion in enhancer-mediated gene activation. *Curr. Opin. Genet. Dev.* **79**, 102022 (2023).

7. C. Michaelis, R. Ciosk, K. Nasmyth, Cohesins: Chromosomal Proteins that Prevent Premature Separation of Sister Chromatids. *Cell* **91**, 35–45 (1997).

8. V. Guacci, D. Koshland, A. Strunnikov, A Direct Link between Sister Chromatid Cohesion and Chromosome Condensation Revealed through the Analysis of MCD1 in S. cerevisiae. *Cell* **91**, 47–57 (1997).

9. F. Uhlmann, D. Wernic, M.-A. Poupart, E. V. Koonin, K. Nasmyth, Cleavage of Cohesin by the CD Clan Protease Separin Triggers Anaphase in Yeast. *Cell* **103**, 375–386 (2000).

10. C. H. Haering, J. Löwe, A. Hochwagen, K. Nasmyth, Molecular Architecture of SMC Proteins and the Yeast Cohesin Complex. *Mol. Cell* **9**, 773–788 (2002).

11. C. H. Haering, A.-M. Farcas, P. Arumugam, J. Metson, K. Nasmyth, The cohesin ring concatenates sister DNA molecules. *Nature* **454**, 297–301 (2008).

12. T. G. Gligoris, J. C. Scheinost, F. Bürmann, N. Petela, K.-L. Chan, P. Uluocak, F. Beckouët, S. Gruber, K. Nasmyth, J. Löwe, Closing the cohesin ring: Structure and function of its Smc3-kleisin interface. *Science* **346**, 963–967 (2014).

13. M. Srinivasan, J. C. Scheinost, N. J. Petela, T. G. Gligoris, M. Wissler, S. Ogushi, J. E. Collier, M. Voulgaris, A. Kurze, K.-L. Chan, B. Hu, V. Costanzo, K. A. Nasmyth, The Cohesin Ring Uses Its Hinge to Organize DNA Using Non-topological as well as Topological Mechanisms. *Cell* **173**, 1508-1519.e18 (2018).

14. D. Ivanov, K. Nasmyth, A Physical Assay for Sister Chromatid Cohesion In Vitro. *Mol. Cell* **27**, 300–310 (2007).

15. N. Zhang, S. G. Kuznetsov, S. K. Sharan, K. Li, P. H. Rao, D. Pati, A handcuff model for the cohesin complex. *J. Cell Biol.* **183**, 1019–1031 (2008).

16. C. Cattoglio, I. Pustova, N. Walther, J. J. Ho, M. Hantsche-Grininger, C. J. Inouye, M. J. Hossain, G. M. Dailey, J. Ellenberg, X. Darzacq, R. Tjian, A. S. Hansen, Determining cellular CTCF and cohesin abundances to constrain 3D genome models. *eLife* **8**, e40164 (2019).

17. S. Xiang, D. Koshland, Cohesin architecture and clustering in vivo. *eLife* **10**, e62243 (2021).

18. K. Tong, R. V. Skibbens, Pds5 regulators segregate cohesion and condensation pathways in Saccharomyces cerevisiae. *Proc. Natl. Acad. Sci.* **112**, 7021–7026 (2015).

19. T. Eng, V. Guacci, D. Koshland, Interallelic complementation provides functional evidence for cohesin–cohesin interactions on DNA. *Mol. Biol. Cell* **26**, 4224–4235 (2015).

20. A. Woglar, K. Yamaya, B. Roelens, A. Boettiger, S. Köhler, A. M. Villeneuve, Quantitative cytogenetics reveals molecular stoichiometry and longitudinal organization of meiotic chromosome axes and loops. *PLoS Biol.* **18**, e3000817 (2020).

21. J. Holzmann, A. Z. Politi, K. Nagasaka, M. Hantsche-Grininger, N. Walther, B. Koch, J. Fuchs, G. Dürnberger, W. Tang, R. Ladurner, R. R. Stocsits, G. A. Busslinger, B. Novák, K. Mechtler, I. F. Davidson, J. Ellenberg, J.-M. Peters, Absolute quantification of cohesin, CTCF and their regulators in human cells. *eLife* **8**, e46269 (2019).

22. S. Rankin, N. G. Ayad, M. W. Kirschner, Sororin, a Substrate of the Anaphase-Promoting Complex, Is Required for Sister Chromatid Cohesion in Vertebrates. *Mol. Cell* **18**, 185–200 (2005).

23. I. P. Mota, M. Galova, A. Schleiffer, T.-T. Nguyen, I. Kovacikova, T. Nishiyama, J. Gregan, J.-M. Peters, P. Schlögelhofer, SORORIN is an evolutionary conserved antagonist of WAPL. doi: 10.21203/rs.3.rs-2199193/v1 (2022).

24. K. A. Nasmyth, B.-G. Lee, M. B. Roig, J. Löwe, What AlphaFold tells us about cohesin's retention on and release from chromosomes. *eLife* **12**, RP88656 (2023).

25. A. L. Lafont, J. Song, S. Rankin, Sororin cooperates with the acetyltransferase Eco2 to ensure DNA replication-dependent sister chromatid cohesion. *Proc. Natl. Acad. Sci.* **107**, 20364–20369 (2010).

26. T. Nishiyama, R. Ladurner, J. Schmitz, E. Kreidl, A. Schleiffer, V. Bhaskara, M. Bando, K. Shirahige, A. A. Hyman, K. Mechtler, J.-M. Peters, Sororin Mediates Sister Chromatid Cohesion by Antagonizing Wapl. *Cell* **143**, 737–749 (2010).

27. R. Ladurner, E. Kreidl, M. P. Ivanov, H. Ekker, M. H. Idarraga-Amado, G. A. Busslinger, G. Wutz, D. A. Cisneros, J. Peters, Sororin actively maintains sister chromatid cohesion. *EMBO J.* **35**, 635–653 (2016).

28. Y. Kim, Z. Shi, H. Zhang, I. J. Finkelstein, H. Yu, Human cohesin compacts DNA by loop extrusion. *Science* **366**, 1345–1349 (2019).

29. F. Ochs, G. Karemore, E. Miron, J. Brown, H. Sedlackova, M.-B. Rask, M. Lampe, V. Buckle, L. Schermelleh, J. Lukas, C. Lukas, Stabilization of chromatin topology safeguards genome integrity. *Nature* **574**, 571–574 (2019).

30. E. Miron, R. Oldenkamp, J. M. Brown, D. M. S. Pinto, C. S. Xu, A. R. Faria, H. A. Shaban, J. D. P. Rhodes, C. Innocent, S. de Ornellas, H. F. Hess, V. Buckle, L. Schermelleh, Chromatin arranges in chains of mesoscale domains with nanoscale functional topography independent of cohesin. *Sci. Adv.* **6**, eaba8811 (2020).

31. J. D. P. Rhodes, J. H. I. Haarhuis, J. B. Grimm, B. D. Rowland, L. D. Lavis, K. A. Nasmyth, Cohesin Can Remain Associated with Chromosomes during DNA Replication. *Cell Rep.* **20**, 2749–2755 (2017).

32. L. Schermelleh, A. Ferrand, T. Huser, C. Eggeling, M. Sauer, O. Biehlmaier, G. P. C. Drummen, Super-resolution microscopy demystified. *Nat. Cell Biol.* **21**, 72–84 (2019).

33. M. Mitter, C. Gasser, Z. Takacs, C. C. H. Langer, W. Tang, G. Jessberger, C. T. Beales, E. Neuner, S. L. Ameres, J.-M. Peters, A. Goloborodko, R. Micura, D. W. Gerlich, Conformation of sister chromatids in the replicated human genome. *Nature* **586**, 139–144 (2020).

34. R. J. Daniels, J. F. Peden, C. Lloyd, S. W. Horsley, K. Clark, C. Tufarelli, L. Kearney, V. J. Buckle, N. A. Doggett, J. Flint, D. R. Higgs, Sequence, structure and pathology of the fully annotated terminal 2 Mb of the short arm of human chromosome 16. *Hum. Mol. Genet.* **10**, 339–352 (2001).

35. J. M. Brown, S. D. Ornellas, E. Parisi, L. Schermelleh, V. J. Buckle, RASER-FISH: non-denaturing fluorescence in situ hybridization for preservation of three-dimensional interphase chromatin structure. *Nat. Protoc.* **17**, 1306–1331 (2022).

36. F. Ochs, K. Somyajit, M. Altmeyer, M.-B. Rask, J. Lukas, C. Lukas, 53BP1 fosters fidelity of homology-directed DNA repair. *Nat. Struct. Mol. Biol.* **23**, 714–721 (2016).

37. L. I. Toledo, M. Altmeyer, M.-B. Rask, C. Lukas, D. H. Larsen, L. K. Povlsen, S. Bekker-Jensen, N. Mailand, J. Bartek, J. Lukas, ATR Prohibits Replication Catastrophe by Preventing Global Exhaustion of RPA. *Cell* **155**, 1088–1103 (2013).

38. D. Gerlich, B. Koch, F. Dupeux, J.-M. Peters, J. Ellenberg, Live-Cell Imaging Reveals a Stable Cohesin-Chromatin Interaction after but Not before DNA Replication. *Curr. Biol.* **16**, 1571–1578 (2006).

39. R. Ciosk, M. Shirayama, A. Shevchenko, T. Tanaka, A. Toth, A. Shevchenko, K. Nasmyth, Cohesin's Binding to Chromosomes Depends on a Separate Complex Consisting of Scc2 and Scc4 Proteins. *Mol. Cell* **5**, 243–254 (2000).

40. I. Psakhye, D. Branzei, SMC complexes are guarded by the SUMO protease Ulp2 against SUMO-chain-mediated turnover. *Cell Rep.* **36**, 109485 (2021).

41. C. Notredame, D. G. Higgins, J. Heringa, T-coffee: a novel method for fast and accurate multiple sequence alignment11Edited by J. Thornton. *J. Mol. Biol.* **302**, 205–217 (2000).

42. Z. E. Smith, D. R. Higgs, The Pattern of Replication at a Human Telomeric Region (16p13.3): Its Relationship to Chromosome Structure and Gene Expression. *Hum. Mol. Genet.* **8**, 1373–1386 (1999).

43. G. Wutz, C. Várnai, K. Nagasaka, D. A. Cisneros, R. R. Stocsits, W. Tang, S. Schoenfelder, G. Jessberger, M. Muhar, M. J. Hossain, N. Walther, B. Koch, M. Kueblbeck, J. Ellenberg, J. Zuber, P. Fraser, J. Peters, Topologically associating domains and chromatin loops depend on cohesin and are regulated by CTCF, WAPL, and PDS5 proteins. *EMBO J.* **36**, 3573–3599 (2017).

44. J. M. Brown, J. Leach, J. E. Reittie, A. Atzberger, J. Lee-Prudhoe, W. G. Wood, D. R. Higgs, F. J. Iborra, V. J. Buckle, Coregulated human globin genes are frequently in spatial proximity when active. *J. Cell Biol.* **172**, 177–187 (2006).

45. R. L. Stallings, D. C. Torney, C. E. Hildebrand, J. L. Longmire, L. L. Deaven, J. H. Jett, N. A. Doggett, R. K. Moyzis, Physical mapping of human chromosomes by repetitive sequence fingerprinting. *Proc. Natl. Acad. Sci.* **87**, 6218–6222 (1990).

46. G. Ball, J. Demmerle, R. Kaufmann, I. Davis, I. M. Dobbie, L. Schermelleh, SIMcheck: a Toolbox for Successful Super-resolution Structured Illumination Microscopy. *Sci. Rep.* **5**, 15915 (2015).

47. A. Matsuda, T. Koujin, L. Schermelleh, T. Haraguchi, Y. Hiraoka, High-Accuracy Correction of 3D Chromatic Shifts in the Age of Super-Resolution Biological Imaging Using Chromagnon. *J. Vis. Exp.*, doi: 10.3791/60800 (2020).

48. A. T. Szczurek, E. Dimitrova, J. R. Kelley, R. J. Klose, Polycomb sustains promoters in a deep OFF-state by limiting PIC formation to counteract transcription. *bioRxiv*, 2023.06.13.544762 (2023).

49. J. Ollion, J. Cochennec, F. Loll, C. Escudé, T. Boudier, TANGO: a generic tool for high-throughput 3D image analysis for studying nuclear organization. *Bioinformatics* **29**, 1840–1841 (2013).

50. R. Haase, L. A. Royer, P. Steinbach, D. Schmidt, A. Dibrov, U. Schmidt, M. Weigert, N. Maghelli, P. Tomancak, F. Jug, E. W. Myers, CLIJ: GPU-accelerated image processing for everyone. *Nat. Methods* **17**, 5–6 (2020).

51. D. Legland, I. Arganda-Carreras, P. Andrey, MorphoLibJ: integrated library and plugins for mathematical morphology with ImageJ. *Bioinformatics* **32**, 3532–3534 (2016).

52. J.-F. Gilles, M. D. Santos, T. Boudier, S. Bolte, N. Heck, DiAna, an ImageJ tool for object-based 3D co-localization and distance analysis. *Methods* **115**, 55–64 (2017).

53. Y. Zhang, T. Liu, C. A. Meyer, J. Eeckhoute, D. S. Johnson, B. E. Bernstein, C. Nussbaum, R. M. Myers, M. Brown, W. Li, X. S. Shirley, Model-based analysis of ChIP-Seq (MACS). *Genome Biology* **9** (2008).

54. A. Kurze, K. A. Michie, S. E. Dixon, A. Mishra, T. Itoh, S. Khalid, L. Strmecki, K. Shirahige, C. H. Haering, J. Löwe, K. Nasmyth, A positively charged channel within the Smc1/Smc3 hinge required for sister chromatid cohesion. *EMBO J.* **30**, 364–378 (2011).

ACKNOWLEDGEMENTS

The authors are grateful to Luke Lavis for generous provision of HaloTag and SNAP-tag dyes. The authors thank Martin Houlard for help with endogenous tagging, Andrew Blackford for advice on co-immunoprecipitations, Jean Metson for laboratory support, and Krzysztof Kus for help with data fitting. The authors wish to thank Mark Willet for access to the Southampton University Imaging Facility, and the Micron Imaging Facility at the University of Oxford for support.

Funding:

Austrian Academy of Sciences, the Vienna Science and Technology Fund (WWTF) projects LS17-003 and LS19-001 (DWG)

Boehringer Ingelheim Fonds PhD fellowship (SK)

Cancer Research UK grant 26747 (KAN)

EMBO Long-Term Fellowship ALTF 1172-2019 (FO)

EPA Cephalosporin Fund CF361 (LS)

European Research Council (ERC) under the European Union's Horizon 2020 research and innovation programme grant 101019039 (DWG)

Independent Research Fund Denmark (DFF) Postdoctoral Fellowship 0164-00011B (FO)

Author contributions:

Conceptualization: FO, KAN

Methodology: FO, VB, JB, ATS, LP, LS

Investigation: FO, CG, JB, VB, SK, DWG

Visualization: FO, CG, SK

Funding acquisition: FO, KAN, DWG, LS, VB

Supervision: KAN

Writing – original draft: FO, KAN

Writing review & editing: all authors

Competing interests: The authors declare no competing interests.

Data and materials availability: MTAs apply to the JF/JFX dyes used in this study (from Luke Lavis) and the pSpCas9(BB)-2A-Puro (PX459) V2.0 plasmid (from Feng Zhang via Addgene). Imaging data and code used in this study have been deposited at Dyrad with the following identifier: doi:10.5061/dryad.3r2280gpg. Imaging data underlying QIBC experiments and RASER-FISH SIM are available from the corresponding authors together with guidance how to navigate them. There are no restrictions on data availability.

SUPPLEMENTARY MATERIALS

Materials and Methods

Figs. S1 to S8

References

Fig.1 Chromatin bound cohesin exists in a monomeric and a dimeric state

(A) Schematic of 3D-SIM imaging approach of endogenously tagged RAD21 in G2 phase and on chromatin. **(B)** Representative widefield and super-resolution 3D-SIM images of chromatin bound RAD21-Halo. Single nucleus z-slice shown or copped region. False coloring by RAD21-Halo signal intensity shows different cohesin populations. **(C)** Frequency distribution of chromatin bound RAD21-Halo signal volumes with fitted non-linear regressions, n> 60.000, RAD21-Halo signals from 2 independent biological experiments. **(D)** Sub-labeling of chromatin bound RAD21-Halo with 50 pM JFX554 dye to achieve single molecule labeling, n> 900 RAD21-Halo signals. **(E)** Photobleaching of sub-labelled RAD21-Halo, example single-step bleach curve is shown corrected for background signal. Quantification in **Fig. S1C**. **(F)** Frequency distribution of single RAD21-Halo molecule volumes obtained from **(D)** and **(E)** was overlaid with frequency distribution of chromatin bound cohesin volumes as shown in **(C)**. Quantification of absolute distributions of chromatin bound cohesin yielded the following frequencies: 22% monomer, 61% dimer, 17% trimer. Quantification is based on non-linear regression analysis. Experiments were carried out in two biological replicates (**B-G**).

Fig.2 Sororin occupies sites of trans chromatid contacts

(A) Analysis strategy to relate distinct pools of cohesin to sister chromatid cohesion, based on published ChIP-Seq data for SMC3 (marker for cohesin) and sororin (*27*) and scsHi-C (*33*) from cells synchronized in G2. In the first step, genomic sites occupied by SMC3 are detected by peak calling in ChIP-Seq data. In step 2, centers of these sites are used to extract neighboring 1 Mb regions of cis (intra-chromatid) and trans (inter-

sister-chromatid) contacts obtained by scsHi-C data. **(B)** Stack-up of SMC3 and sororin log2 normalized ChIP-Seq signals for a 6-kb window around SMC3 peak centers for SMC3 sites with sororin signal higher than 0.1 CPM (SMC3 with sororin). SMC3 and sororin ChIP-Seq data are from G2 wild type samples, from two biological replicates (*27*). **(C)** Stack-up of SMC3 and sororin log2 normalized ChIP-Seq signals for a 6-kb window around SMC3 peak centers for sites with sororin signal lower than 0.1 CPM (SMC3 without sororin). SMC3 and sororin ChIP-Seq data are from G2 wild type samples, data from two biological replicates (*27*). **(D)** Average cis sister and trans sister observed/expected values around centers of SMC3 peaks with sororin in G2 synchronized cells. Data are merged from n=11 biologically independent experiments. Averaged contact maps were computed using 10 kb genomic bins. **(E)** Average cis sister and trans sister observed/expected values around centers of SMC3 peaks without sororin in G2 synchronized cells. Data are merged from n=11 biologically independent experiments. Averaged contact maps were computed using 10 kb genomic bins. **(F)** Stack-up of trans sister observed/expected values within 100 kb sliding window around SMC3 peak centers for SMC3 with sororin in a 1 Mb window. For SMC3 peaks with sororin, the average observed/expected value for trans contacts calculated in a 100 kb window around the SMC3 peak center is 1.31 ± 1.05. Data is from G2 synchronized cells analyzed in **(B)** and **(D)**. **(G)** Stack-up of trans sister observed/expected values within 100 kb sliding window around SMC3 peak centers for SMC3 without sororin in a 1 Mb window. For SMC3 peaks with sororin, the average observed/expected value for trans contacts calculated in a 100 kb window around the SMC3 peak center is 0.92 ± 0.93. Data is from G2 synchronized cells analyzed in **(C)** and **(E)**.

Fig.3 Cohesin complexes associated with sororin specifically mark sites of sister chromatid cohesion

(A) Schematic depiction of RASER-FISH approach for imaging of sites of sister chromatid cohesion. Two possible outcomes are shown; the cohesed sister chromatids are visible as one FISH signal or non-cohesed sister chromatids are visible as “split dots” due to their spatial separation. This figure was made with Biorender.com. **(B)** Frequencies of “split dots” (separated sister chromatids) measured by FISH and conventional microscopy in G2 cells. Probe locations are midpoints of cosmids in kb from chromosome 16 p telomere. TA; human lymphoblastoid cell line established from a normal individual, MEJY JY5.4; mouse erythroleukaemia hybrid cell line containing a normal human chromosome 16. N> 200 alleles analyzed per cosmid, averaged from 2 independent biological repeats. **(C)** RASER-FISH outcomes of two probes, marking sites of sister chromatid cohesion are shown, ether in wildtype conditions or conditions of cohesin loss induced by PROTAC3-mediated degradation of RAD21 (8h treatment). G2 cells were identified by sororin mean intensity (wild type) or Cyclin A mean intensity (no cohesin). Example images of G2 cells shown (left) and quantification shown (right). Experiments were carried out in biological duplicates. N=57 HS443D9 WT, n=43 HSD443D9 no cohesin, n=28 HS306A4 WT and n=31 HS306A4 no cohesin. Kruskal-Wallis test yielded p=0.0095, mean and standard deviation (SD) are plotted. **(D)** Co-localization of sororin to cohesed (top) and non-cohesed (bottom) sites and absolute

quantification of sororin occupancy of the respective sites. Samples were prepared under pre-extraction conditions to visualize sororin, which maintained cohesion. Experiments were carried out in biological duplicates. N=48 HS443D9 (top), n=28 HSD443D9 (bottom), n=31 HS306A4 (top) and n=20 HS306A4 (bottom). Kruskal-Wallis test yielded p=0.0075 (top) and p=0.0086 (bottom), mean and SD are plotted. **(E)** Distance analysis between sister chromatids (distance between intensity maxima) at sites occupied by or void of sororin. Experiments were carried out in biological duplicates and n=49 for sororin positive sites and n=55 for sororin negative sites. Mann-Whitney U test yielded p<0.000001, mean and SD are plotted. Graphs are artificially jittered in x to show distributions.

Fig.4 Sororin is a monomer and associated with <1/3 of chromatin bound cohesin

(A) Schematic depiction of 3D-SIM imaging approach of endogenously tagged RAD21 together with sororin in G2 phase and on chromatin. **(B)** Representative widefield and 3D-SIM images of chromatin bound sororin. Single nucleus z-slice shown or cropped region shown. False coloring by sororin signal intensity shows uniform population. **(C)** Frequency distribution of chromatin bound sororin signal intensities with fitted non-linear regression (Gaussian distribution); SumInt; Sum Intensity; A.U., arbitrary units, n> 140.000 sororin signals from two biologically independent experiments. **(D)** Frequency distribution of signal intensities of chromatin bound sororin in **Fig. 4C** is overlaid with non-specific antibody conjugate intensities observed on imaging slides outside nuclei as shown in **(E)**. N>3700 antibody conjugates and data are from two biologically independent experiments. **(E)** Example image showing analysis of single sororin intensities. On imaging slides, primary and secondary antibody conjugates, which occur through non-specific binding, were segmented, and their frequency distribution analyzed. Arrows indicate non-specific antibody conjugates on slide (blue) and specific sororin signals (green). Antibody specificity in cells has been controlled for in **Fig. S5A**. Quantification of absolute distributions of chromatin bound sororin from **Fig. 4C** yielded the following frequencies: 74.4% (monomer), 15.75% (dimer) and 9.85% (multimer). Quantification is based on non-linear regression analysis. **(F)** Example image of RAD21-Halo and sororin colocalization in G2 phase cells. Maximum projections of 5 z-slices are shown, as entire nucleus and cropped region. Overlaps are indicated in white circles and numbered lines mark the normalized intensity profiles show measurements. **(G)** Colocalization analysis of RAD21 at sites of sister chromatid cohesion marked by sororin. Bar charts consist of dots, each representing an analyzed RAD21 signal. Colocalization was analyzed in two biologically independent experiments with >38.000 RAD21 molecules analyzed per repeat. Absolute numbers for RAD21 colocalization with sororin are 28.47% (repeat 1) and 28.56% (repeat 2). Two-tailed student t-test determined p<0.0001, means are shown.

Fig.5 Sister chromatid cohesion is maintained by individual cohesin rings

(A) Schematic depiction of labeling approach. U2OS RAD21-Halo cells were incubated with two different HaloTag ligands, each labeling ~50% of RAD21-Halo (see **Fig. S7A-C** for controls) The table shows expected frequencies of observing one Halo dye at a

sororin site, or the other, or both at the same time, for monomeric, dimeric and multimeric cohesin. **(B)** Example 3D-SIM image of G2 cell after incubation with JFX554 and JFX650 against RAD21-Halo (each labeling ~50%) and immunostaining with sororin antibody. A single z-slice of a nucleus is shown and quantification in **(D)** and **(H)**. **(C)** Examples of classes I-III (sororin-containing signals) detected in G2 cells. Single z-slices of 3D-SIM example crops are shown. **(D)** Quantification of **(C)**. Three-way colocalization was measured in two biologically independent experiments, with 1200 sororin sites analyzed per repeat. Means are 8.21% (sororin without RAD21-Halo), 45.00% (sororin with RAD21-Halo JFX554), 44.46% (sororin with RAD21-Halo JFX650) and 2.33% (sororin with RAD21-Halo JFX554 and RAD21-Halo JFX650). Dots represent individual cells. Statistical testing by two-tailed student t-test yielded $p<0.000001$. **(E)** Examples of classes IV-VI (cohesin at sororin absent sites) detected in G2 cells. Single z-slices of 3D-SIM example crops are shown. **(F)** Cohesin at sites without sororin was analyzed in two biologically independent experiments, with 1200 cohesin signals analyzed per repeat. Means are 26.67% (2 x RAD21-Halo JFX554), 24.79% (2 x RAD21-Halo JFX650) and 48.54% (RAD21-Halo JFX554 and RAD21-Halo JFX650). Dots represent individual cells. Statistical testing by two-tailed student t-test yielded $p<0.000001$. **(G)** RASER-FISH example of probe HS443D9 co-localizing with RAD21-Halo in a dye mixing experiment (left) and quantification (right). N=34 probe signals from two biologically independent experiments. Mann-Whitney U test yielded $p=0.33$.

Science
AAAS

Supplementary Materials for

Sister chromatid cohesion is mediated by individual cohesin complexes

Fena Ochs*, Charlotte Green, Aleksander Tomasz Szczurek, Lior Pytowski, Sofia Kolesnikova, Jill Brown, Daniel Wolfram Gerlich, Veronica Buckle, Lothar Schermelleh and Kim Ashley Nasmyth*

*Corresponding author: fena.ochs@bric.ku.dk and ashley.nasmyth@bioch.ox.ac.uk

The PDF file includes:

Materials and Methods

Sequence alignments

The following NCBI reference sequences were used to generate the SMC3 alignments: NP_113771.2 (*H. sapiens*), NP_031816.2 (*M. musculus*), NP_989848.1 (*G. gallus*), XP_031761083.1 (*X. tropicalis*), NP_999854.1 (*D. rerio*), NP_523374.2 (*D. melanogaster*), NP_593260.1 (*S. pombe*), NP_982360.1 (*E. gossypii*), QEU58755.1 (*K. lactis*), XP_446916.1 (*C. glabrata*), NP_012461.1 (*S. cerevisiae*).

Sequences were aligned using T-Coffee (*41*) with conserved and similar residues highlighted using Boxshade (https://github.com/mdbaron42/pyBoxshade/releases).

Cell culture

Tissue culture of EBV cell line TA and the mouse hybrid cell line with a normal human chromosome 16 (MEL JY5.4) was as previously described (*42*). U2OS osteosarcoma cells (gift from Benjamin Rowland) were grown in DMEM containing 10% heat-inactivated FBS and penicillin-streptomycin antibiotics. The following endogenously tagged cell lines were used in this study: U2OS cells with RAD21 C-terminally tagged with HaloTag (RAD21-Halo) (*31*), U2OS RAD21-Halo cells with SMC3 tagged with an internal Spot-Tag (SMC3-E602-Spot), U2OS RAD21-Halo, SMC3-E602-Spot cells with sororin C-terminally tagged with a SNAP-tag (sororin-SNAP). All cell lines were routinely tested to confirm mycoplasma-free status using a LookOut Mycoplasma PCR Detection Kit (Sigma-Aldrich).

Cell lines

All genetically modified cell lines generated for this study were obtained using CRISPR/Cas9 endogenous tagging. Cells were transfected with the pSpCas9(BB)-2A-Puro (PX459) V2.0 plasmid (kindly provided by Feng Zhang via Addgene, #62988) expressing Cas9 and guide RNAs as well as with a donor plasmid containing the insert, linker and homology arms using Lipofectamine 2000 (Invitrogen, 11668019). Transfected cells were selected under Puromycin (1 μg/ml) and after 7 days plated at single cell density. Homozygous cell lines were obtained by colony picking, PCR screening and validated by western blotting, Sanger sequencing and immunofluorescence. For U2OS RAD21-Halo, SMC3-E602-Spot the following guide RNA was used: ACTCACATTGGTTTCAGGAT. The insert flanked by 7 amino acid linkers was: GGGSGGG-Spot-GGGSGGG. 200 base pair homology arms were used and sequencing primers were: GGCAACATAGGGAGACCCTG (forward) and CTGTCTCCCTCCCCAAAACC (reverse). For sororin-SNAP tagging, the following guide RNA was used: CCACTGCATCTCATTCAACC. The insert flanked by a 5 amino acid linker was: GGSGG-SNAP$_f$,, 600 base pair homology arms were used, and the sequencing primers were: GAAGACTTGTCCGGAGTCTCG (forward) and CCCACGAATTCTCTCTGGGAC (reverse).

Gene silencing by RNA interference

Transfection of siRNAs (Ambion Silencer Select) was performed with Lipofectamine RNAiMAX (Thermo Fisher Scientific, 13778075) at a final concentration of 20 nM. For single transfections, cells were transfected, medium exchanged after 6 h and cells incubated for 72 h. For double transfections, cells were transfected on two consecutive days, medium exchanged after 6 h and cells incubated for a total of 96 h. siRNAs used targeted CDCA5/sororin (#1 s41424; #2 s41426). siRNAs against PDS5A and PDS5B have been published before (*43*). Ambion negative control #1 was used as control siRNA.

Antibodies, nanobodies and fluorescent ligands for immunofluorescence and western blotting

The following primary antibodies were used: sororin (rabbit, Abcam, ab192237, 1:250 for QIBC, 1:100 for SIM, 1:500 for WB), MCM2 (mouse, Novus Biologicals, H00004171-M01, 1:500 for QIBC), RAD21 (mouse, Merck Millipore, 05-908, 1:250 for SIM, 1:500 for WB), SMC3 (rabbit, Cell Signaling, 5695, 1:1000 for WB), SMC1a (rabbit, Abcam, ab9262, 1:500 for WB), Lamin-B1 (rabbit, Abcam, ab133741, 1:500 for WB), Spot-tag (mouse, ChromoTek, 1:50 for IF), Cyclin A (mouse, Santa Cruz, sc-271682, 1:100 for IF). The following primary nanobody was used: Spot VHH (llama, Chromotek, etb-250, 1:200 for WB). Secondary-antibody conjugates for immunofluorescence staining were goat-anti mouse and goat anti-rabbit Alexa Fluor 488 (A11029; A11034; 1:1000 for QIBC and SIM), Alexa Fluor 568 (A11031; A11306; 1:1000 for QIBC and SIM) and Alexa Fluor 647 (A21236; A21245; 1:1000 for QIBC and SIM) reagents (Invitrogen, highly cross-adsorbed). Secondary antibodies for WB were ECL sheep anti-mouse IgG, HRP-linked F(ab')2 fragment (Fisher Scientific UK, 10106134, 1:5000 for WB), ECL donkey anti-rabbit IgG, HRP-linked F(ab')2 fragment (Fisher Scientific UK, 10710965; 1:5000 for WB) and goat anti-llama IgG (H+L) HRP (Thermo Fisher, A16060; 1:5000 for WB). Fluorescent ligands used were HaloTag JF479, HaloTag JFX554, HaloTag JFX650 and SNAP-Tag JF549 and JF552 (all gifts from Luke Lavis). Final concentrations for HaloTag ligands were 100 mM unless otherwise indicated. Final SNAP-Tag ligand concentration was 5 mM.

SDS-Page, western blotting and in-gel detection

SDS-PAGE was performed using 4-12% Bis-Tris gels and Mini Gel Tanks from Thermo Fisher. Western blotting was carried out using Bio-Rad wet transfer systems. Membranes were stained with antibodies as indicated above and developed using chemiluminescence (Amersham ECL detection reagent, RPN2134). For SMC3-E602-Spot and SMC1-ALFA WBs, custom 8% Bis-Tris midi gels were run for 18 h at 4°C before wet transfer. For in-gel detection, SDS-PAGE gels were detected on a FLA7000 biomolecular imager. For dye titration, cells were incubated with decreasing amounts of dye, samples run of SDS-PAGE, detected in-gel and band intensities quantified using FLA7000 analysis software.

Co-Immunoprecipitation

Lysates for immunoprecipitations were prepared from U2OS cells by washing in phosphate-buffered saline (PBS) and lysis in IP buffer (100 mM NaCl, 0.2% Igepal Ca-630, 1 mM $MgCl_2$, 10% glycerol, 5 mM NaF, 50 mM Tris-HCl, pH 7.5) supplemented with cOmplete EDTA-free protease inhibitor cocktail and 25 U/ml Benzonase. After nuclease digestion, NaCL and EDTA concentrations were adjusted to 150 mM and 2 mM respectively and unless otherwise stated. Lysates were incubated with 1 mg antibody/mg lysate for 1 h with end-to-end mixing at 4°C. Afterwards, samples were incubated with protein G magnetic agarose beads for 2 h with end-to-end mixing at 4°C.

Immunofluorescence staining

Cells were grown to 80% confluency on 22x22 mm #1.5H high-precision coverslips (thickness 0.170 ± 0.005 mm, Marienfeld Superior). Cells were washed in PBS, pre-extracted in ice-cold PBS 0.2% Triton X-100 (Sigma-Aldrich) for 1.5 min on ice and fixed in 4% formaldehyde for 15 min. For non-pre-extracted samples, cells were fixed and subsequently permeabilized in PBS 0.2% Triton X-100 for 5 min. Primary and secondary antibodies were diluted in antibody diluent (DMEM medium containing 10% FBS, 0.05% sodium azide, sterile filtered 0.2 mm). Samples were incubated in primary antibody for 1.5 h and for 1 h in secondary antibody solution supplemented with 4',6'-diamidino-2-phenylindole-dyhydrochloride (DAPI, 0.5 mg/ml). In between primary and secondary antibody staining, samples were washed 3x in PBS 0.2% Tween. After secondary antibody incubation, samples were washed 3x again, samples were post-fixed in 4% formaldehyde for 15 min and samples were washed in PBS and distilled water. For QIBC, samples were mounted in Mowiol-based mounting medium (Mowiol 488 (Calbiochem)/glycerol/Tris-HCl, pH 8.5) and in non-hardening Slowfade Diamond (Thermo Fisher Scientific, S36963) for Spinning Disk and 3D-SIM imaging. For EdU staining, cells were incubated with 10 mM EdU 20 min before pre-extraction and EdU detection was performed before primary antibody incubation according to the manufacturer's instructions (Thermo Fisher Scientific). For detection of endogenously tagged proteins with chemical dyes, samples were incubated for 1.5 h with Halo- or 3 h with SNAP-ligands, washed three times in fresh media and incubated for 30 min in the incubator in fresh media for exit wash of unbound dye. For experiments with two Halo dyes, cells were incubated with both dyes for 1.5 h, then washed and chased with a third dye as indicated. For calibration purposes, U2OS cells were incubated with 100 nm 4-colour Microspheres (fluorescent blue, green, orange, dark red; Thermo Fisher Scientific) for 3 days at a density of 30 μl bead slurry / $2x10^5$ cells. For G2 analysis, cells with highest mean intensities for Cyclin A (fixed cells) or sororin (pre-extracted cells) were chosen.

DNA FISH

Methanol-acetic acid–fixed cells were prepared and hybridized as described in (*44*). Hybridized slides were examined using a fluorescence microscope (Olympus BX60). Hybridization efficiency was assessed by scoring FITC signals in ten metaphase spreads and only those hybridizations with greater than 80% efficiency were scored. 200 FITC signals were scored as either single or split dots for each hybridization. The percentage

of split dot values for each cosmid plotted represent the average of two independent biological experiments.

RASER-FISH

RASER-FISH allows DNA sequence detection in intact 3D cell nuclei as it maintains fine-scale chromatin structure by replacement of heat denaturation with exonuclease III digestion after UV-generation of DNA nicks. RASER-FISH was carried out as described in (*29*, *35*). In brief, U2OS cells were seeded on 22x22 mm #1.5H high-precision coverslips (thickness 0.170 ± 0.005 mm) and labelled for 18 h with 10 μM BrdU/BrdC mix (3:1). Cells were either pre-extracted and fixed as described above or fixed in 4% formaldehyde and permeabilized in PBS 0.2% Triton-X-100 for 5 min. Immunofluorescence staining for sororin or Cyclin A was carried out as described above. After incubation with 0.5 μg/ml DAPI for 15 min for UV sensitization, cells were treated with UV light (254 nm) for 15 min followed by incubation with 5 U/μl exonuclease III (NEB) at 37°C for 15 min. Biotin labelled probes were denatured in hybridization mix at 90°C for 10 min, pre-annealed with human Cot-1 DNA (Invitrogen) at 37°C for 15 min and hybridized to samples overnight at 39°C. Coverslips were washed twice in 1x SSC buffer at 37°C for 30 min, once in 1x SSC at room temperature, once in PBS, and biotin was detected by incubation with streptavidin-Alexa488 (1:500, Thermo Fisher). Samples were post-fixed, rinsed in PBS and MilliQ and mounted in Slowfade Diamond. For RAD21 degradation, cells harboring RAD21-Halo were incubated with 2.5 μM HaloPROTAC3 (Promega) for the last 8 h of BrdU/BrdC incubation. For dye mixing experiments, dye mixing was carried out as described above for the last 2 h of BrdU/BrdC incubation. The probes for all FISH assays in this study were obtained from a chromosome 16p specific cosmid library based on genome assembly NCBI36 (*45*) and have been characterized in (*34*) for mapping of the terminal 2 Mb of chromosome 16 p-arm. The GenBank accession number for the entire map is AE005175 and the specific probes used in this study have EMBL IDs HS306A4 (AL008727) and HS443D9 (Z92845). Probes were biotin-labelled.

Quantitative image-based cytometry (QIBC)

QIBC (*36*, *37*) was performed on a motorized Olympus IX83 inverted wide-field microscope equipped with Semrock DAPI/FITC/Cy3/Cy5 Quad LED filter set, Hamamatsu Orca Fusion B CMOS camera and Lumencor SPECTRA X light source. Automated unbiased image acquisition was carried out with the proprietary ScanR acquisition software. Identical exposure times were used for all samples within one experiment and settings were chosen for maximum dynamic range under non-saturating conditions. Most data was obtained with the Olympus UPLXAO 20x, NA 0.8 air objective. Depending on cell confluency and type of image analysis, 49-100 images were acquired, aiming for at least 2000 cells per analysis after gating. After acquisition, images were analyzed using the ScanR analysis software. DAPI signal was used for segmentation of nuclei based on intensity threshold. This nucleus mask was then used to quantify pixel intensities in the different channel for each individual nucleus. After segmentation and pixel quantification, measured parameters were extracted (mean and total intensities,

area, circularity, well). For automated vermicelli quantification, edge detection was used, and 4 arbitrary classes were defined based on increasing edges (none, mild, moderate, and severe chromatin compaction). All data were exported to Tibco Spotfire, which was used to quantify average/median values in cell populations and to generate color-coded scatter plots in a flow-cytometry fashion, or to GraphPad Prism to generate stacked bar charts.

Spinning disk microscopy

Representative pseudo-confocal images were acquired with an UltraView Vox spinning-disk microscope (Perkin Elmer) and Volocity software (version 6.3.1) with a 60x, 1.42 NA Plan-Apochromat oil-immersion objective. Images were captured with a Hamamatsu EMCCD 16-bit camera at a spatial resolution of 121x250 nm. Single z-slices of whole nuclei are shown, brightness and contrast were linearly adjusted for optimal display. Color-channels were false-colored.

Structured illumination microscopy (SIM)

3D-SIM images were acquired with a DeltaVision OMX SR system (GE Healthcare) equipped with a 60x, 1.5 NA UPLAPO60XOHR oil immersion objective (Olympus), pco.edge 4.2 sCMOs cameras (PCO), and 405 nm, 488 nm, 568 nm and 640 nm lasers. 3D image stacks were acquired over the whole nuclear volume in z with 15 raw images per plane (3 angles, 5 phases). Spherical aberration was minimized using immersion oil with refractive index 1.514 and an objective collar setting of 0.140 for image acquisition. Raw data was computationally reconstructed with SoftWoRx 7.2.0 (GE Healthcare) using channel-specific optical transfer functions (OTFs) recorded using immersion oil with RI 1.516 and Wiener filter setting 0.0030. All SIM data were routinely and meticulously quality-controlled for effective resolution and absence of artifacts using SIMcheck (*46*). Multichannel acquisitions were aligned in 3D with Chromagnon software (*47*) using 3D-SIM acquisitions of multicolor EdU-labelled C127 cells as colocalization reference. Images were thresholded based on the MCNR function of SIMcheck, which generates a metric of local stripe modulation contrast in different regions of the raw data and directly correlates this with the level of high-frequency information content in the reconstructed data. Only immunofluorescent signals with underlying MCNR values that exceeded a stringent quality threshold were considered for further analysis, while localizations with low underlying MCNR values were discarded. Thereby, any SIM signal, which falls below reconstruction confidence and is considered to be a labelling/imaging artifact, is excluded from further data interpretation (*46*). For representative images, single z-slices, cropped regions of whole nuclei or partial z-stacks are shown as indicated in figure legends. Brightness was linearly adjusted for optimal presentation. Channels were false-colored.

HILO photobleaching

Cells were seeded and labelled on 35 mm diameter, No. 1.5 MatTek dishes, pre-extracted and fixed as described above, and imaged in PBS. For photobleaching, a custom-built total internal reflection fluorescence (TIRF) microscope (described in detail in (*48*)) was

used with a 100x 1.4 NA oil objective (Olympus) and with an iChrome MLE MultiLaser engine (Topica Photonics). Photobleaching was performed using highly inclined laminar optical sheet illumination (HILO). Emission was projected onto the central region of an iXon 897 EMCCD camera (Andor, 512x512 pixels). Pixel size in acquired images was 96 nm. Sample position and focus were controlled with a motorized stage and z-motor (ASI). For photobleaching samples were exposed to 30 % (RAD21-Halo) and 10-20% (sororin-SNAP) 561 nm laser and imaged using 100 ms camera interval for up to 1.5 min. Obtained images were analyzed with the Fiji plugin "Time Series Analyser" (https://imagej.nih.gov/ij/plugins/time-series.html) and background subtraction over time was performed using parallel background measurements.

SIMinspector

SIMinspector is a custom image analysis tool for the segmentation of sub-cellular features and analysis of colocalization in multicolor 3D-super-resolution microscopy images. SIMinspector code can be downloaded from Dyrad with the identifier doi:10.5061/dryad.3r2280gpg.

SIMinspector consists of 2 Fiji scripts that are explained below and can be executed in the following order:

1. **SIMinspector_Mainobject_Fiji:** This Fiji script segments the main object, e.g. cell nucleus, based on intensity thresholding. For this, a selected channel ("Channel for mask creation") is used. Objects are detected based on intensity thresholding ("Threshold method") and all objects but the largest are excluded. It produces segmented and cropped 3D images in the specified output directory.
2. **SIMinspector_Subobject_Fiji:** This Fiji script segments subobjects from 2 channels, measures volumes, intensities and centers as well as colocalization based on voxel overlap, center-to-center distances and center-to-edge distances. To this end, images are made isotropic and channels are thresholded ("Segmentation algorithm"). Maxima are detected ("Maxima radius") and made into labels. Maxima-derived labels were used for marker-controlled intensity-based watershed filtering. Optional, resulting labels can be eroded to optimize segmentation ("Label erosion channel"). Afterwards images were resliced and objects below minimum and above maximum volumes excluded ("Minimum spot volume in voxels", "Maximum spot volume in voxels"). Resulting stacks are converted to 16-bit, original pixel sizes restored, and statistics of labels computed. Computed centers of mass are mapped. Fiji's plugin DiAna (*15*) is used to calculate voxel overlaps, center-to-center and center-to-edge distances for the N nearest neighbors. The script produces 4 .csv files. The file ending on "StatisticsOfLabelmap_C1" contains all measurements for channel 1, the file ending on "StatisticsOfLabelmap_C2" contains all measurements for channel 2 and the files "AdjacencyResults_C1vsC2" contain the colocalization results originating from either center of mass or geometric center values.

The dependencies for these scripts are 3D ImageJ Suite(*49*), Java 8, CLIJ (*50*), CLIJ2, clijx-assistant, clijx-assistant extension, IJPB (*51*) and DiAna (*52*).

SMC3 and sororin ChIP-Seq heatmaps

ChIP-Seq data for SMC3 and sororin from (*27*) (https://www.ebi.ac.uk/ena/browser/view/PRJEB12214) were mapped using bwa (v0.7.17) against human genome assembly GRCh37/hg19. Raw read counts were normalized to counts per million (CPM) values and log-transformed using a base two logarithm. The peaks were called using macs2 (*53*) using a p-value threshold of $1e^{-10}$. For each detected SMC3 peak the average sororin signal was measured using pybbi package version 0.3.2 (https://github.com/nvictus/pybbi). SMC3 peaks with a mean sororin signal higher than 0.1 CPM were marked as "SMC3 with sororin" (20943 peaks). The remaining SMC3 peaks were marked as "SMC3 without sororin" (13848 peaks). Heatmap plots centered at SMC3 sites with or without sororin were calculated using a custom ipython notebook. Samples come from wild type HeLa Kyoto cells synchronized to G2, and from two biological replicates. SMC3 and sororin ChIP-Seq data from (*27*) can be accessed in the European Nucleotide Archive (ENA) with the accession number PRJEB12214.

Hi-C aggregate maps

Scs-Hi-C data for wild type HeLa Kyoto cells synchronized in G2 (GSE152373) were processed as described in (*33*). Observed-over-expected scsHi-C aggregate maps were calculated using the cooltools package version 0.5.4 (https://github.com/open2c/cooltools). 1 Mb ICE-corrected snippets around SMC3 sites with or without sororin ("observed") were extracted and each value in the snippets was normalized by the value of the scaling at that diagonal ("expected"). The pixel-wise average across the snippet was then calculated. The main diagonal and one neighboring diagonal were blanked out to avoid Hi-C artefacts. G2 maps were constructed from 1.7 billion Hi-C reads with 195 million unique reads from 11 biological repeats. HeLa scsHi-C data from (*33*) can be access at Gene Expression Omnibus (GEO) with accession number GSE152373.

Stack-up analysis of line profiles for ChIP-Seq and scsHi-C data

Stack-ups of line profiles within 1 Mb windows centered at SMC3 sites with or without sororin were calculated using a custom iPython notebook. The contact density within a sliding diamond of 100 kbs was calculated along each region within the set of regions of length m for observed-over-expected matrices, resulting in a vector of size n for each region. Then, these vectors were stacked into an m × n matrix with m denoting the number of regions and n denoting the length of the line profile along each region. For display of observed-over-expected values, a pseudocount of 0.01 was added before log-transformation. Line profiles containing only invalid Hi-C bins were removed from the stack-up. Code underlying ChIP and scs-HiC analysis, can be downloaded from Dyrad with the identifier doi:10.5061/dryad.3r2280gpg.

Statistics and reproducibility

Sample size was not pre-determined. Sample size, statistical tests and the number of biological replicates for each experiment are indicated in the figure legends. Two-tailed student t-test was used to test Gaussian distributed data in **Fig. 4G**, **Fig. 5D, Fig. 5F** and **Fig. S4C**. Mann-Whitney U test was used to test ranks in **Fig. 3E**, **Fig. 5G,** and **Fig. S1C**, **Fig. S5C**, **Fig. S6H**. Kruskal-Wallis test was used to test ranks between more than 2 groups in **Fig.3C, Fig. 3D** and **Fig. S3H**.

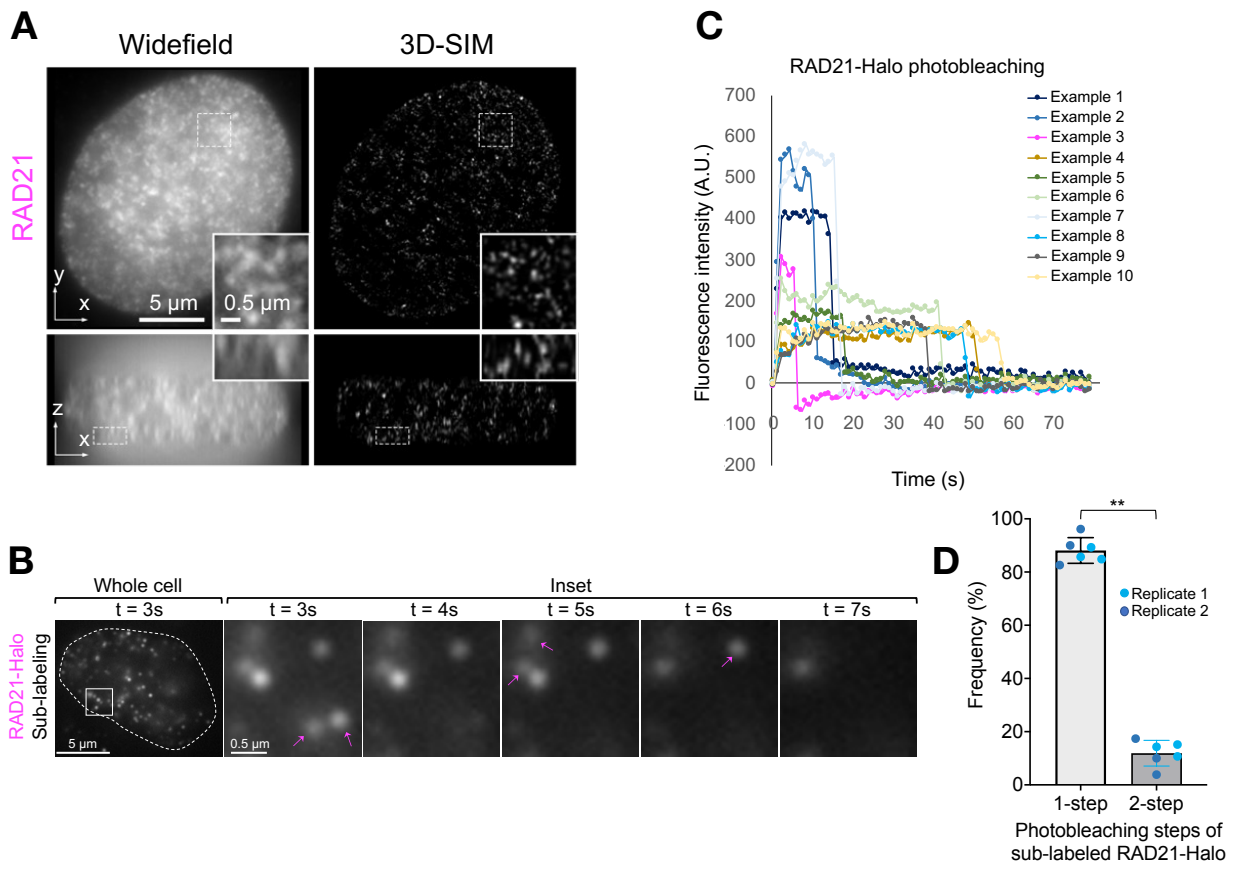

Fig. S1 Molecular counting of chromatin bound RAD21-Halo

(A) Representative widefield and super-resolution 3D-SIM images of chromatin bound RAD21-Halo as shown in **Fig. 1B** with added orthogonal views for illustration of 3D resolution increase by SIM. Single nucleus z-slice shown or copped region. **(B)** HILO-photobleaching of sub-labeled chromatin bound RAD21-Halo. Example cell nucleus with sparse RAD21-Halo signals is shown as well as crops at consecutive time points to visualize single step bleach reactions of events (highlighted with magenta arrows). **(C)** Quantification of single step-wise photobleaching of 10 example signals of chromatin bound RAD21-Halo after sub-labeling. Data is background corrected using regions of identical sizes. Bleaching occurs at different timepoints due to Gaussian nature of HILO laser beam. **(D)** Quantification of steps in bleach events observed in RAD21-Halo after sub-labeling and on chromatin. The experiment was carried out in two independent biological repeats with >90 bleach reactions analyzed per repeat. Dots indicate independent technical repeats per biological repeat. Mann-Whitney U test yielded p=0.0022.

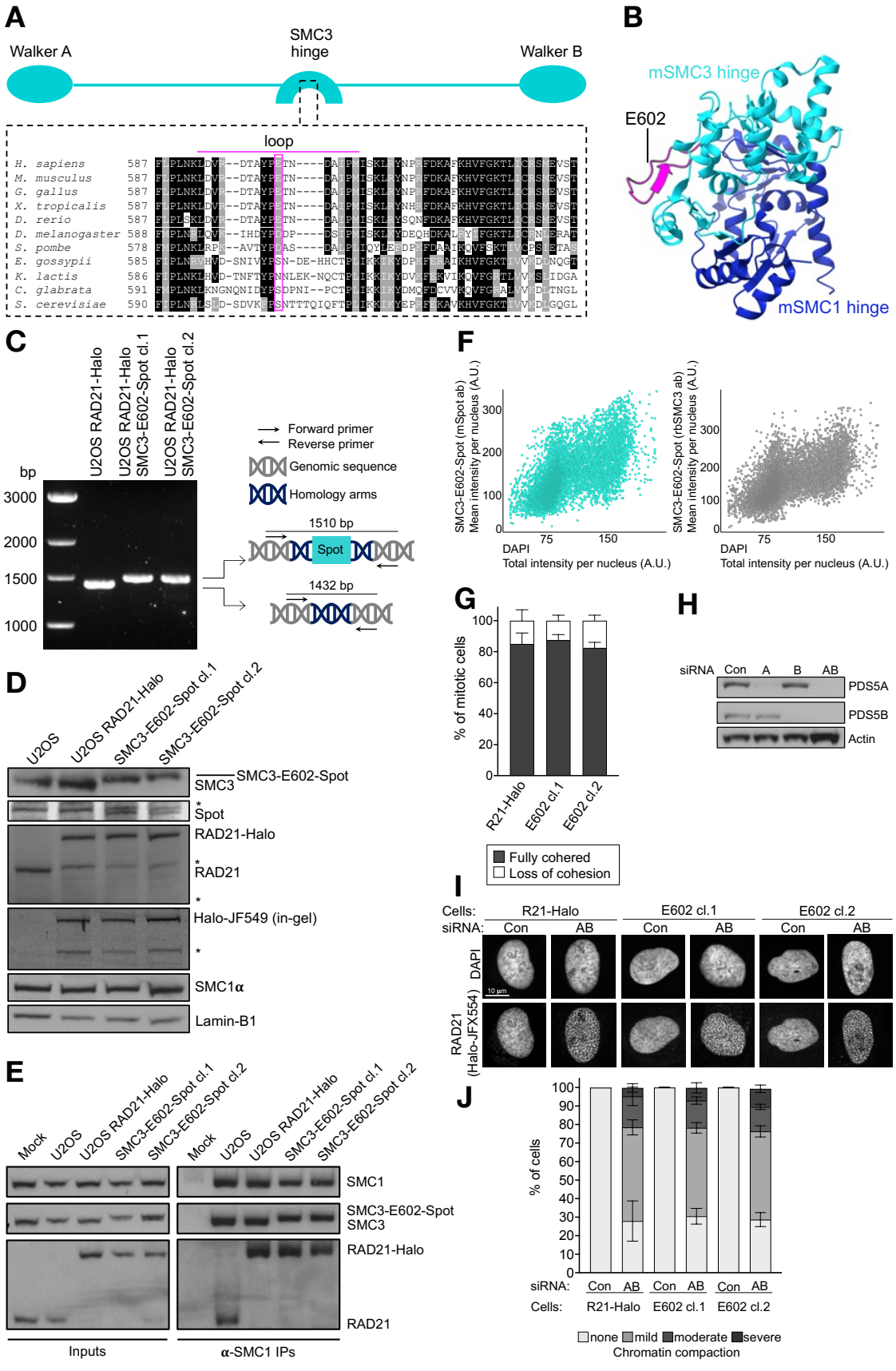
A
Walker A
SMC3 hinge
Walker B
loop
H. sapiens 587
M. musculus 587
G. gallus 587
X. tropicalis 587
D. rerio 587
D. melanogaster 588
S. pombe 578
E. gossypii 585
K. lactis 586
C. glabrata 591
S. cerevisiae 590
B
mSMC3 hinge
E602
mSMC1 hinge
C
U2OS RAD21-Halo
U2OS RAD21-Halo SMC3-E602-Spot cl.1
U2OS RAD21-Halo SMC3-E602-Spot cl.2
bp
3000
2000
1500
1000
Forward primer
Reverse primer
Genomic sequence
Homology arms
1510 bp
Spot
1432 bp
D
U2OS
U2OS RAD21-Halo
SMC3-E602-Spot cl.1
SMC3-E602-Spot cl.2
SMC3
SMC3-E602-Spot
Spot
RAD21-Halo
RAD21
Halo-JF549 (in-gel)
SMC1α
Lamin-B1
E
Mock
U2OS
U2OS RAD21-Halo
SMC3-E602-Spot cl.1
SMC3-E602-Spot cl.2
SMC1
SMC3-E602-Spot
SMC3
RAD21-Halo
RAD21
Inputs
α-SMC1 IPs
F
SMC3-E602-Spot (mSpot ab) Mean intensity per nucleus (A.U.)
SMC3-E602-Spot (rbSMC3 ab) Mean intensity per nucleus (A.U.)
DAPI
Total intensity per nucleus (A.U.)
G
% of mitotic cells
R21-Halo
E602 cl.1
E602 cl.2
Fully cohered
Loss of cohesion
H
siRNA Con A B AB
PDS5A
PDS5B
Actin
I
Cells:
siRNA:
R21-Halo
E602 cl.1
E602 cl.2
Con
AB
DAPI
RAD21 (Halo-JFX554)
10 μm
J
% of cells
siRNA: Con AB Con AB Con AB
Cells: R21-Halo E602 cl.1 E602 cl.2
none
mild
moderate
severe
Chromatin compaction

Fig. S2 Generation of cell line for endogenously tagged cohesin complex

(A) Sequence alignment for SMC3 hinge region from H. sapiens to *S. cerevisiae* colored by amino acid conservation (60% threshold). The loop targeted for endogenous tagging surrounding amino acid residue E602 is highlighted in magenta. **(B)** *M. musculus* cohesin hinge with loop targeted for endogenous tagging of SMC3 highlighted in magenta (PDB: 2WD5) (*54*)**(C)** PCR showing homozygous tagging of SMC3-E602 with Spot-tag in two independent clones. **(D)** Western blot of SMC3-E602-Spot clones 1 and 2 compared to parental cell lines to show homozygous tagging. Membrane was immunostained for Spot, RAD21, SMC1 and Lamin-B1. Halo-tag was detected in-gel with JF549 and SMC3 was detected on overnight midi-gel to visualize 1.4 kDa size difference of Spot-tag insertion. **(E)** IP of SMC3-E602-Spot clones 1 and 2 by α-SMC1 antibody, immunostained for SMC1, SMC3 and RAD21. Input is 1% total sample. **(F)** Scatter plots showing the cell cycle distribution pattern of chromatin bound SMC3 detected in the endogenously tagged SMC3-E602-Spot cell line with Spot antibody (left) versus the cell cycle distribution pattern of chromatin bound SMC3 detected with SMC3 antibody in RAD21-Halo cells. m; mouse, rb; rabbit, ab; antibody. N=9700, the experiment was repeated twice biologically independently. **(G)** Quantification of metaphase spreads in RAD21-Halo parental cells and SMC3-E602-Spot clones 1 and 2. Spreads were counted as fully cohered, and railroad as well as prematurely separated chromosomes were counted as loss of cohesin phenotype. Two biologically independent experiments were carried out, with >20 metaphase spreads analyzed per cell line and repeat. Mean and SD are shown. **(H)** Western blot showing siRNA depletion efficiency of PDS5A and B in RAD21-Halo U2OS cells. Vermicelli were induced by combined siRNA depletion of PDS5A and B. **(I)** Example images of RAD21-Halo and SMC3-E602-Spot clones 1 and 2 after control or PDS5A/B siRNA treatment. RAD21-Halo was visualized in all cell lines by JFX554 dye and DNA by DAPI staining. Images were acquired with a spinning disk microscope and false-colored. **(J)** Vermicelli were categorized as wild type, mild, moderate and severe chromatin compaction phenotypes by automated ScanR analysis. Mean and SD are shown. Two biologically independent experiments were carried out, with >1000 cells analyzed per cell line, condition and repeat.

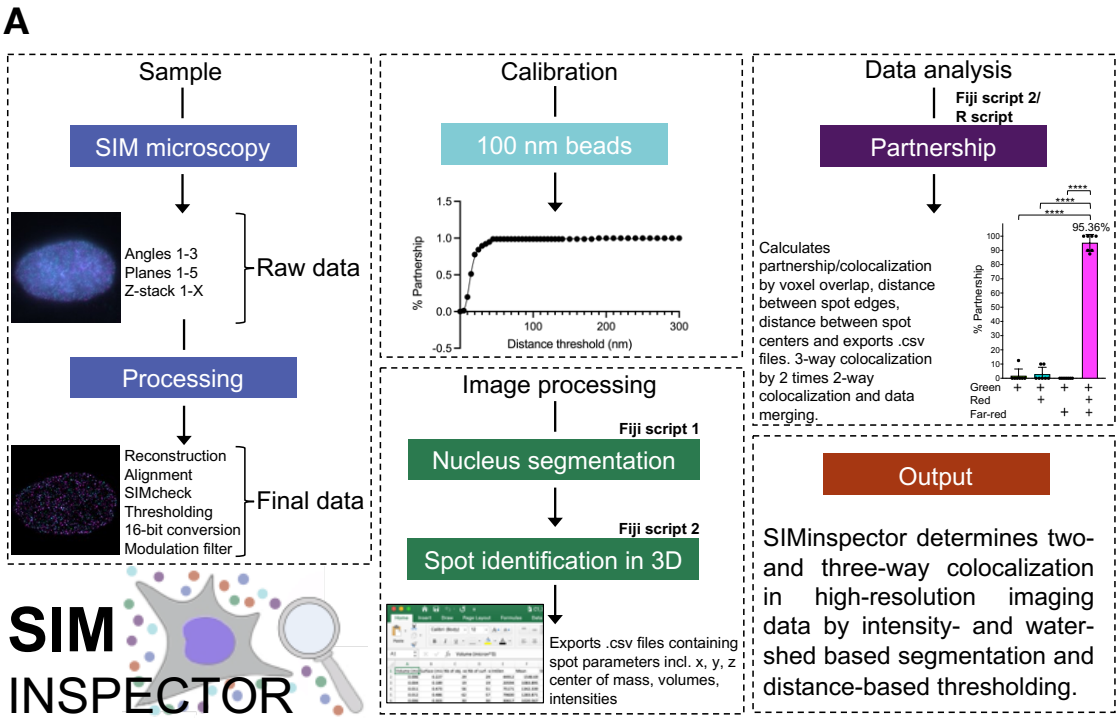
A
Sample
SIM microscopy
Angles 1-3
Planes 1-5
Z-stack 1-X
Raw data
Processing
Reconstruction
Alignment
SIMcheck
Thresholding
16-bit conversion
Modulation filter
Final data
SIM
INSPECTOR
Calibration
100 nm beads
% Partnership
Distance threshold (nm)
Image processing
Fiji script 1
Nucleus segmentation
Fiji script 2
Spot identification in 3D
Exports .csv files containing spot parameters incl. x, y, z center of mass, volumes, intensities
Data analysis
Fiji script 2/
R script
Partnership
Calculates partnership/colocalization by voxel overlap, distance between spot edges, distance between spot centers and exports .csv files. 3-way colocalization by 2 times 2-way colocalization and data merging.
95.36%
Green
Red
Far-red
Output
SIMinspector determines two- and three-way colocalization in high-resolution imaging data by intensity- and water-shed based segmentation and distance-based thresholding.

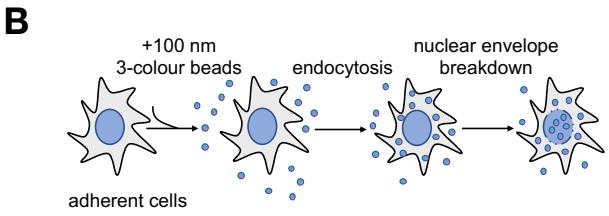
B
+100 nm
3-colour beads
endocytosis
nuclear envelope
breakdown
adherent cells

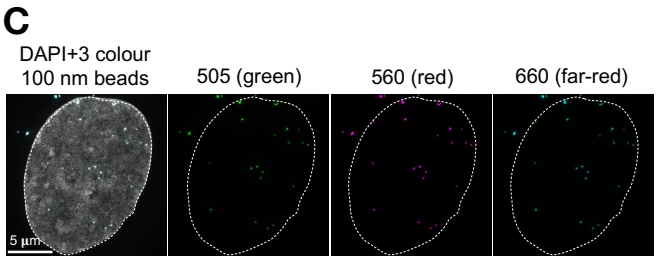
C
DAPI+3 colour
100 nm beads
505 (green)
560 (red)
660 (far-red)
5 µm

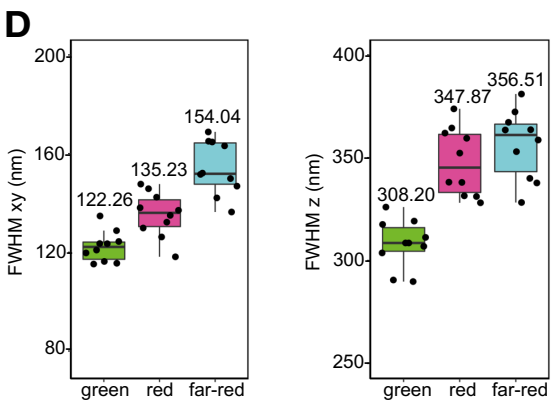
D
FWHM xy (nm)
200
160
120
80
154.04
135.23
122.26
green
red
far-red
FWHM z (nm)
400
350
300
250
356.51
347.87
308.20
green
red
far-red

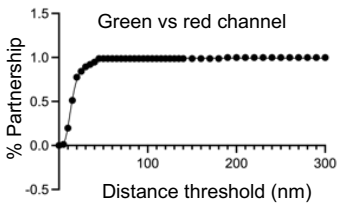
E
Green vs red channel
% Partnership
Distance threshold (nm)
Green vs far-red channel
% Partnership
Distance threshold (nm)

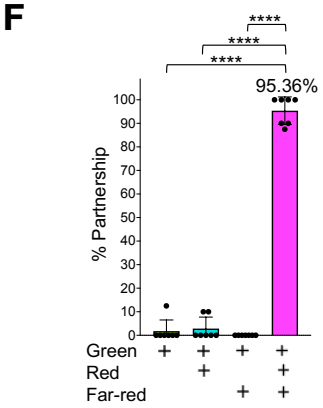
F
****
****
****
95.36%
% Partnership
Green
Red
Far-red

Fig S3 SIMinspector, an image analysis tool for 3D super-resolution microscopy

(A) Schematic depiction of the SIMinspector workflow. 3D-SIM images are acquired and processed. Calibration samples are analyzed to determine microscope- and sample-specific parameters. Script 1 (SIMinspector_mainobject_Fiji) segments the main object based on intensity thresholding. Script 2 (SIMinspector_subobject_Fiji) segments subobjects by intensity thresholding and watershedding and exports intensity, volume, pairwise colocalization measurements and center positions. 3-way colocalization is determined by 2x two-way colocalization. **(B)** For calibration, U2OS cells were incubated with 100 nm 3-colour beads for 48 hours, which led to nuclear incorporation. This allowed calibration measurements in same cellular environment as actual samples. **(C)** Example 3D-SIM images of DAPI stained nucleus with incorporated 3-colour beads (5 slice maximum projection). **(D)** Full width at half maximum (FWHM) measurements in lateral and axial dimensions for monomeric beads within U2OS cells for all 3 channels, n=10 single bead signals, shown are median (middle line) and interquartile range (IGQ; box), whiskers are 1.5* IQR. **(E)** Measurement of two-way colocalization between green and red emission signals (left) and between green and far-red emission signals (right) detected from three-color 100 nm beads at a varying distance threshold, solid line represents sigmoid fit. N=80 beads. **(F)** Three-way colocalization analysis of beads within U2OS cells. At 99 nm distance threshold, >95% of bead signals from 3 channels colocalize. N=80 beads, experiment was carried out twice biologically independently. Kruskal-Wallis test determined $p<0.0001$, mean and SD are shown.

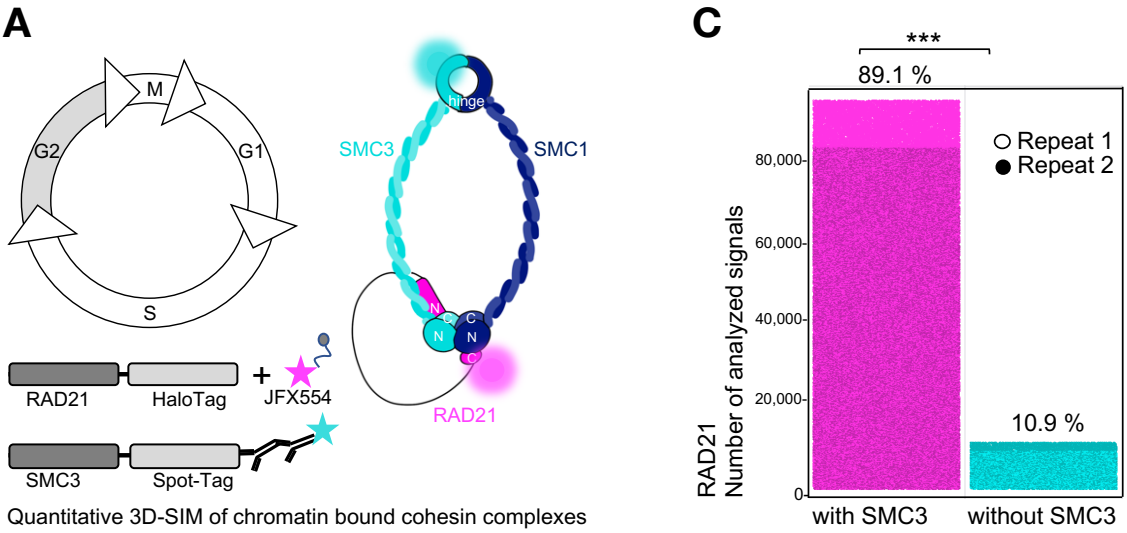
A
M
G2
G1
S
RAD21
HaloTag
JFX554
SMC3
Spot-Tag
hinge
SMC3
SMC1
RAD21
Quantitative 3D-SIM of chromatin bound cohesin complexes
C
***
89.1 %
10.9 %
Repeat 1
Repeat 2
RAD21
Number of analyzed signals
80,000
60,000
40,000
20,000
0
with SMC3
without SMC3

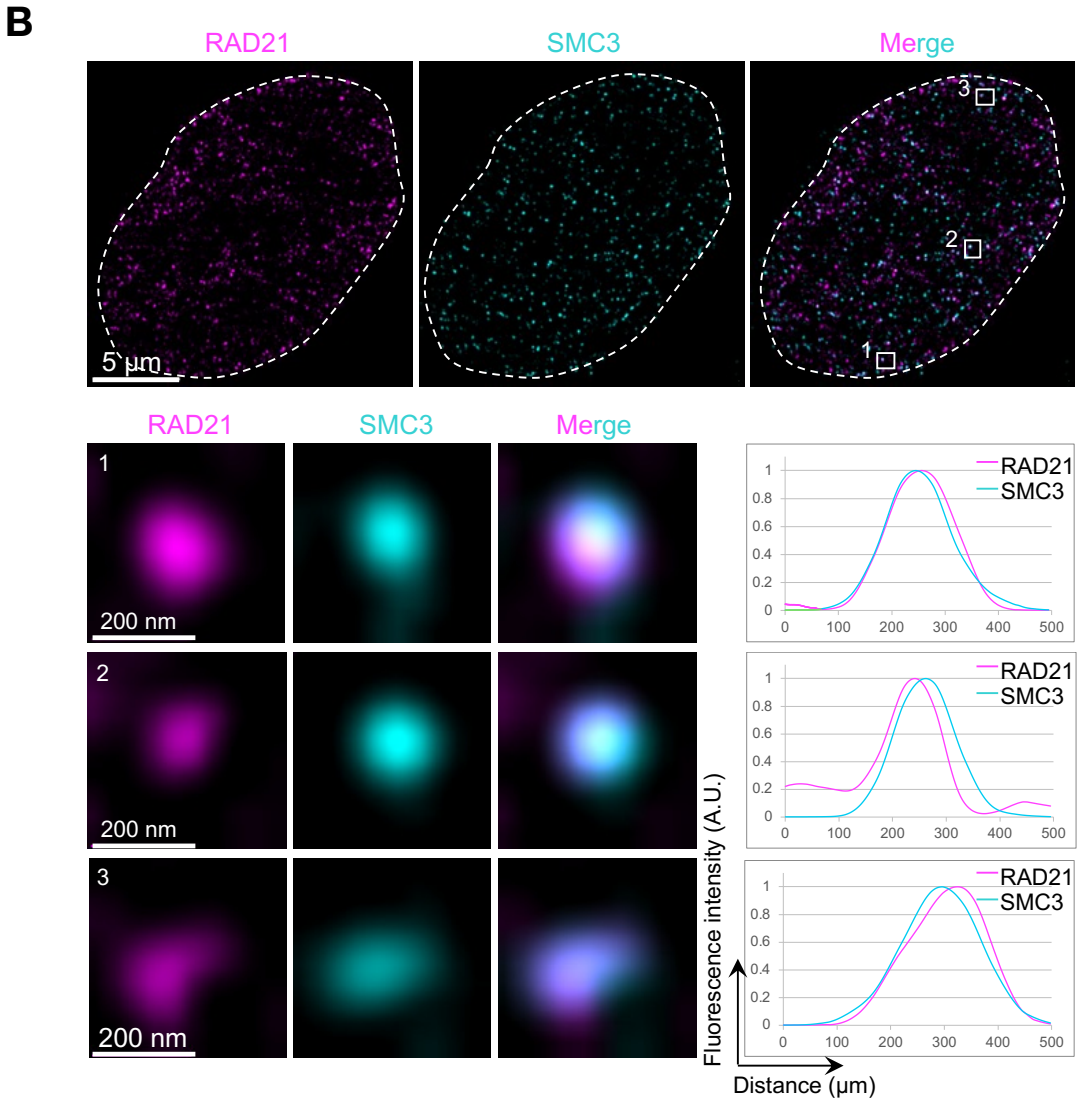
B
RAD21
SMC3
Merge
5 µm
1
2
3
200 nm
Fluorescence intensity (A.U.)
Distance (µm)

Fig. S4 Chromatin bound RAD21 marks cohesin complexes

(A) Schematic depiction of 3D-SIM imaging approach of endogenously tagged cohesin complexes in G2 phase and on chromatin. RAD21 is Halo-tagged and SMC3 Spot-tagged at the cohesin hinge. **(B)** Chromatin-bound cohesin visualized by 3D-SIM microscopy, nucleus shown as single z-slice, colocalization shown in cropped regions of single z-slices and intensity line profiles. RAD21-Halo was visualized by incubation with JFX554 dye and SMC3-E602-Spot with Spot antibody. Images were false colored. **(C)** Quantification of colocalization between RAD21-Halo and SMC3-E602-Spot as detected in **(B)**. 2 biologically independent repeats are shown in overlay, single spots represent single RAD21-Halo signals analyzed. N>90.000 analyzed RAD21 signals per repeat, the experiment was repeated twice in biologically independent manner. Statistical testing by two-tailed student t-test yielded p=0.0004.

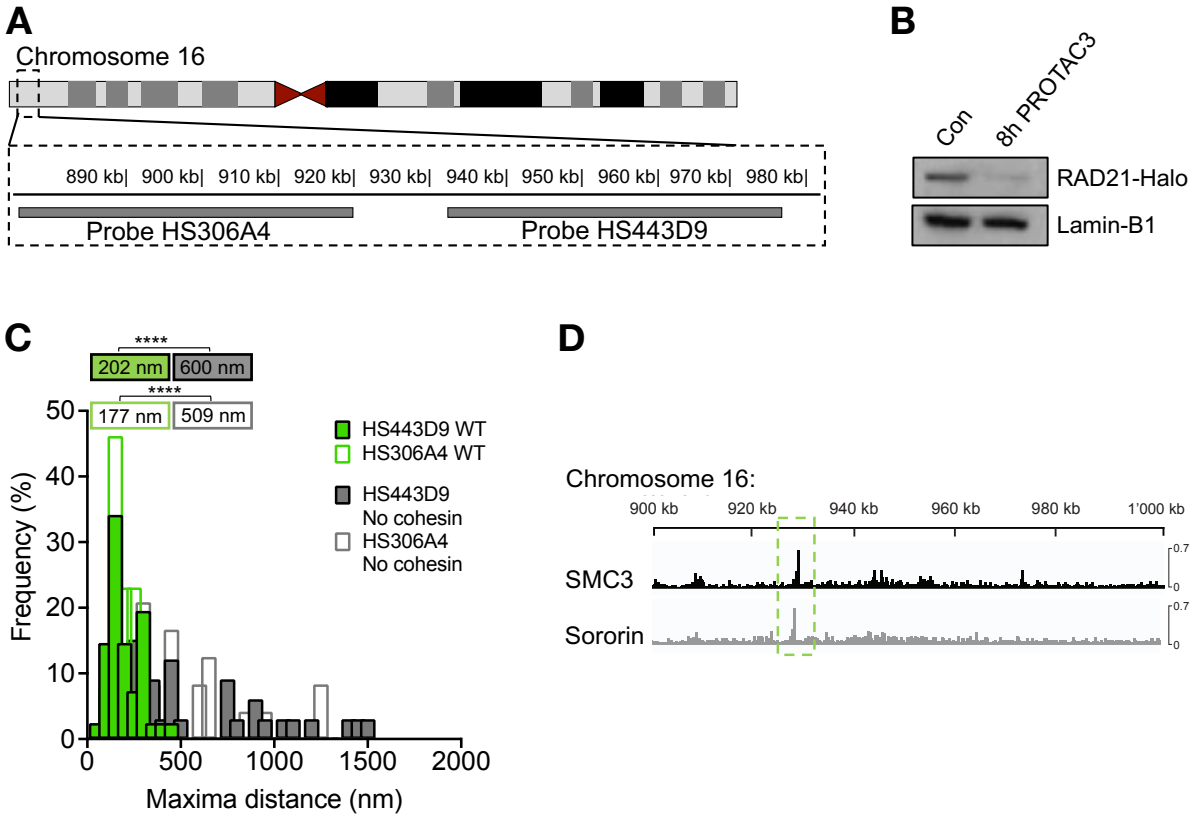

Fig S5 Sites of sister chromatid cohesion can be visualized by RASER-FISH

(A) Locus on human chromosome 16 p-arm. A 320 kb window was identified with highest proximity of sister chromatids by cosmid-contig tiling of the terminal 3.5 Mb of the chromosome arm. Two probes HS306A4 and HS443D9 from this 320 kb region were used in this study to visualize sites of sister chromatid cohesion. **(B)** Western blot showing degradation of cellular RAD21-Halo by 8 h treatment with 2.5 μM PROTAC3. Lamin-B1 is used as loading control. **(C)** Distance measurements between sister chromatids labelled with either probe HS306A4 or HS443D9 in wild type or no cohesin conditions. N=41 HS443D9 WT, n=34 HSD443D9 no cohesin, n=13 HS306A4 WT and n=24 HS306A4 no cohesin. Mann-Whitney U test yielded $p<0.000004$, mean values for each probe in WT and no cohesin conditions are shown. **(D)** ChIP-Seq profiles of SMC3 and sororin in HeLa cells along a 100 kb region on chromosome 16 from ChIP-Seq data (*27*) corresponding to the region of interest identified by RASER-FISH.

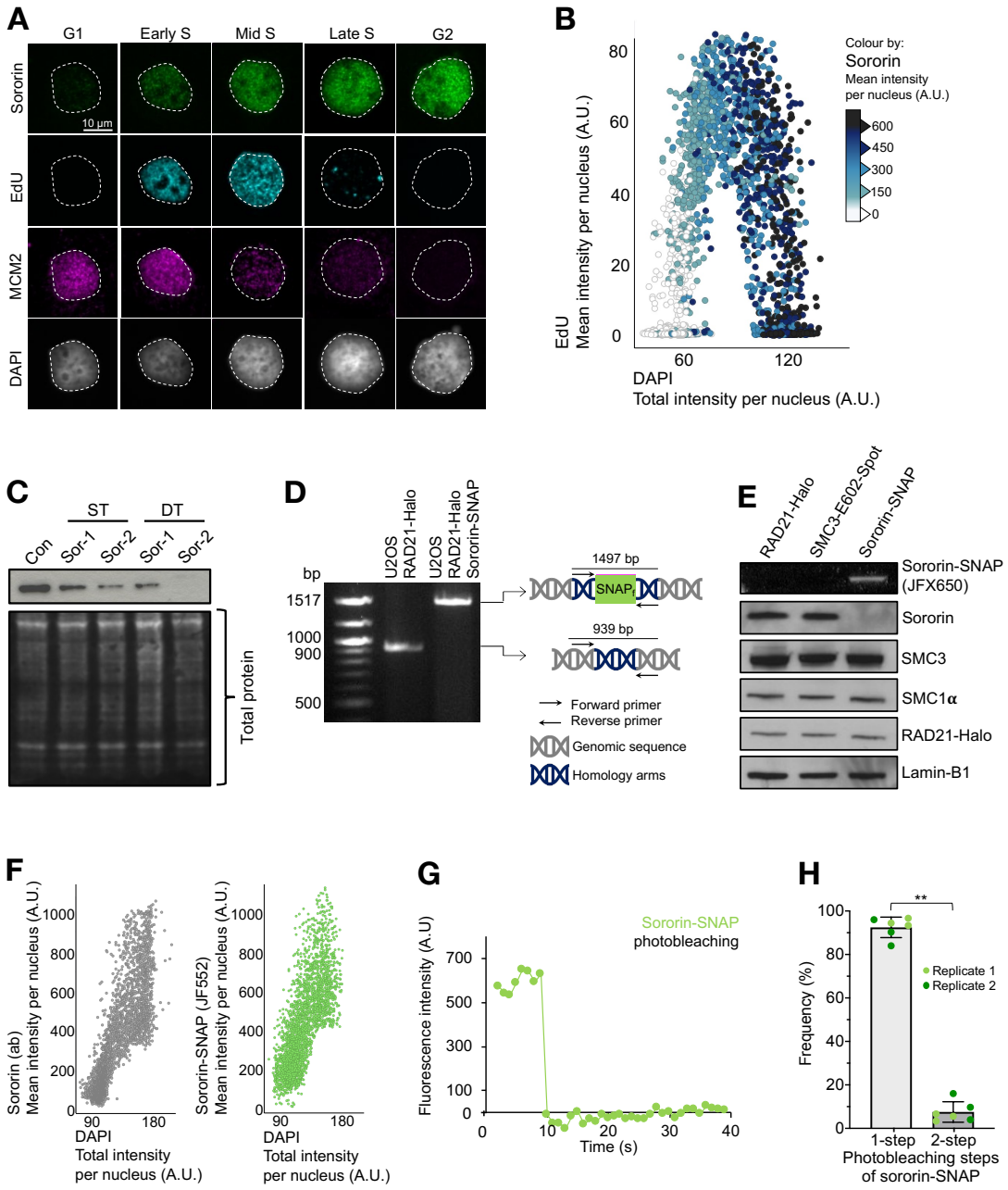

Fig S6 Sororin is a monomer and its recruitment to chromatin coupled to DNA replication

(A) Cell cycle analysis of sororin binding to chromatin by immunofluorescence. Cell cycle stages were identified based on EdU (5-ethynyl-2'-deoxyurdine, thymidine analogue, S phase marker), MCM2 antibody (marker for pre-replicative chromatin) and DAPI (DNA marker). Example images for each cell cycle stage were acquired on a Spinning Disk microscope and quantification shown in **(B)**. Cells were false-colored. **(B)** QIBC of chromatin bound sororin. Scatter plots shows single cells as dots over cell cycle by plotting of EdU over DAPI nuclear intensities. This delineates G1 phase (bottom left cloud with 2N DNA), S phase cells (arch) and G2 phase cells (bottom right cloud with 4N DNA).

The color code shows the mean intensity of chromatin bound sororin signal per cell. 3400 cells are shown, the experiment was repeated twice in a biologically independent manner. **(C)** Western blot of sororin depletion from U2OS wild type cells with two independent siRNAs (Sor-1 and Sor-2) over 72 or 96 h, with immunostaining for sororin and total protein extract. ST, single transfection; DT; double transfection; Con, control siRNA; Sor-1, siRNA1 against sororin; Sor-2; siRNA2 against sororin. **(D)** PCR showing homozygous tagging of sororin with SNAP-tag. **(E)** Western blot showing endogenous tagging of sororin with SNAP-tag. Western blot was immunostained for Lamin-B1, RAD21, SMC1, SMC3, sororin and sororin-SNAP detected in gel with JFX650. Cell lines used were U2OS RAD21-Halo (RAD21-Halo), U2OS RAD21-Halo SMC3 E602-Spot (SMC3-E602-Spot), U2OS RAD21-Halo, SMC3-E602-Spot, sororin-SNAP (sororin-SNAP). **(F)** QIBC analysis of sororin antibody (left) and endogenously tagged sororin-SNAP (right) serves as antibody specificity control. 3500 cells are shown per condition. The experiment was repeated twice independently. **(G)** Example of 1-step photobleaching of chromatin bound sororin-SNAP incubated with JF549 by HILO. **(H)** Quantification of photobleaching of chromatin bound sororin-SNAP incubated with JF549 dye. The experiment was carried out in two independent biological repeats with >80 bleach reactions analyzed per repeat. Dots indicate independent technical repeats per biological repeat. Mann-Whitney U test determined p=0.002165, mean and SD are shown.

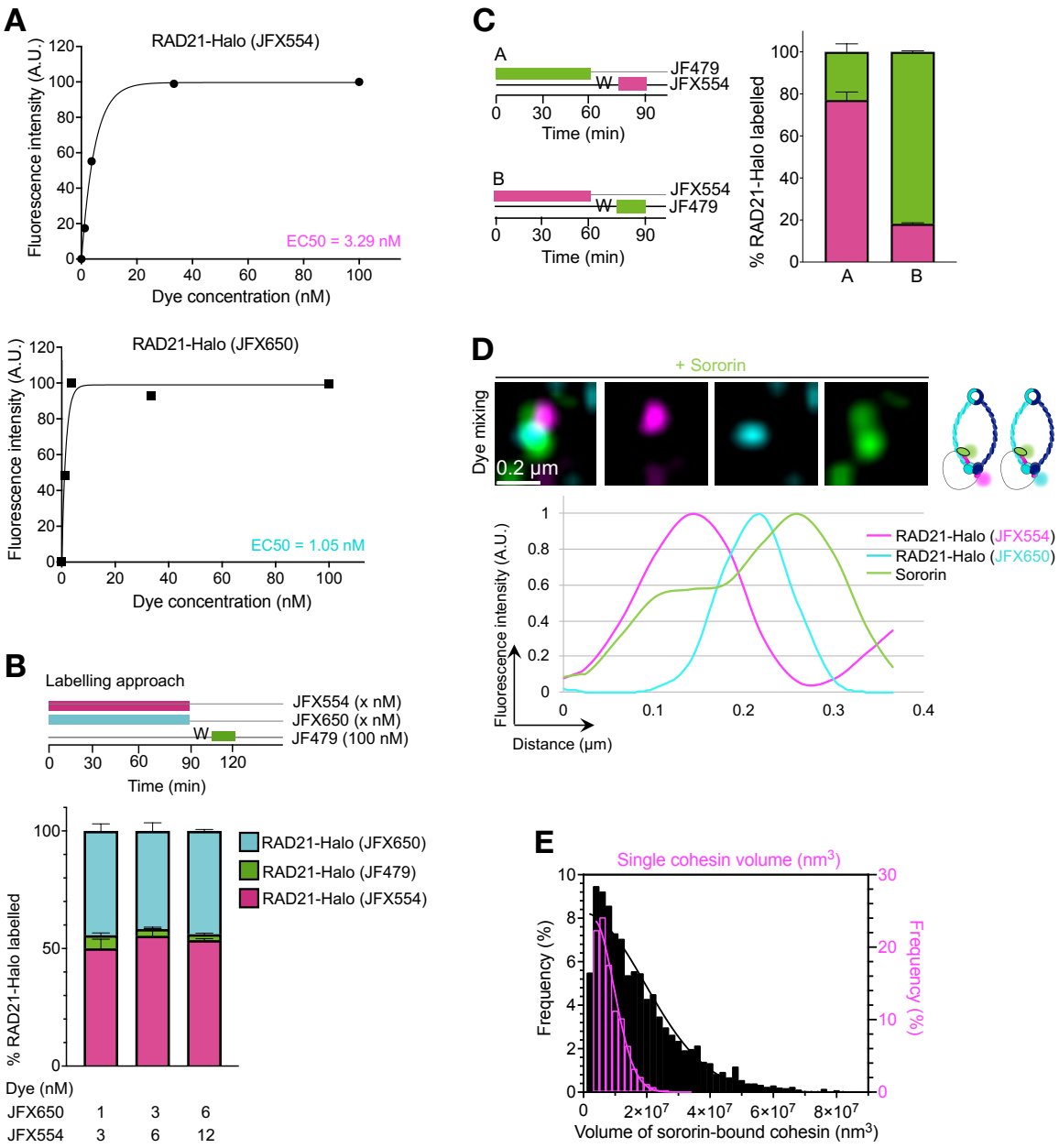

Fig S7 HaloTag dyemixing allows molecular counting

(A) Titration of RAD21-Halo dyes JFX554 and JFX650 in U2OS RAD21-Halo cells. EC50 was determined to 3.29 nM (JFX554) and 1.05 nM (JFX650). **(B)** Labeling approach (top) and quantification of signal frequencies (bottom). Samples were incubated with varying concentrations of mixed dyes JFX554 and JFX650 for 1.5 h, washed and chased with a third dye JF479. Samples were imaged with 3D-SIM and single RAD21-Halo signals analyzed. N>28.000 RAD21-Halo analyzed per condition. W; wash. Mean and SD are shown. **(C)** To validate labeling efficiency of JF479 dye used for chasing in **Fig. S7B**, cells were incubated with dye JFX554 for 1 h, chased by JF479 and vice versa. RAD21-Halo labelling frequency was obtained from normalized intensity distributions for n>4000 cells

imaged by QIBC. The experiment was repeated twice in a biologically independent manner. W; wash. Mean and SD are shown. **(D)** 3D-SIM image crop of 2 sororin signals overlapping with two RAD21-Halo molecules, one labelled with JFX554 (magenta) and one labelled with JFX 650 (cyan). A single z-slice is shown and intensity quantification below. **(E)** Overlay of frequency distribution of chromatin bound RAD21 monomer volumes shown in **Fig. 1F** with volumes of sororin-associated RAD21. N>33.000 sororin-cohesin complexes and the experiment was carried out twice in biologically independent manner.

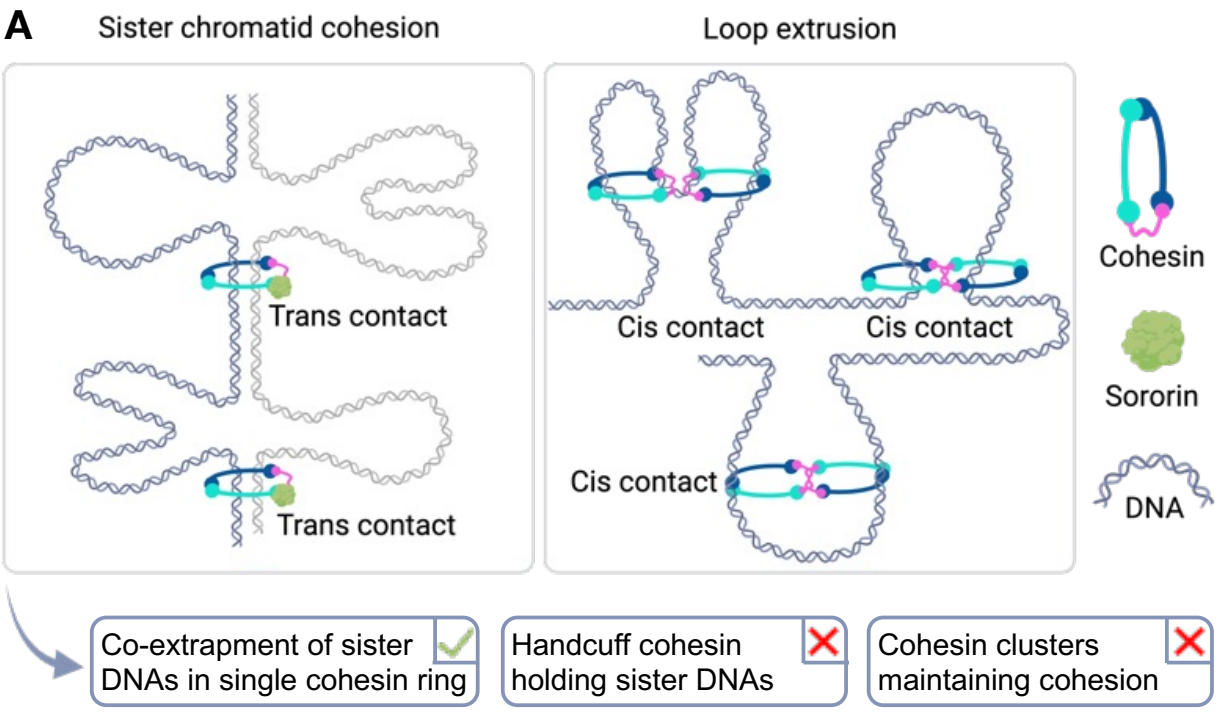

Fig S8 A model for chromatin organization by cohesin.

(A) Cis and trans chromatin organization are mediated by discrete cohesin populations. Sister chromatid cohesion is mediated by a monomer of cohesin bound to a single sororin molecule and constitutes around a third of chromatin bound cohesin in G2. Non-cohesive chromatin bound cohesin in G2 constitutes the remaining two thirds of cohesin and appears dimeric. This could be spatially coupled cohesin complexes or truly linked dimers. This figure was made with Biorender.com.